Journal of Magnetic Resonance 202 (2010) 43–56

Contents lists available at ScienceDirect

Journal of Magnetic Resonance

journal homepage: www.elsevier.com/locate/jmr

A tensor model and measures of microscopic anisotropy for double-wave-vector diffusion-weighting experiments with long mixing times

Marco Lawrenz, Martin A. Koch, Jürgen Finsterbusch *

Department of Systems Neuroscience, University Medical Center Hamburg-Eppendorf, Hamburg, Germany
Neuroimage Nord, University Medical Centers Hamburg-Kiel-Lübeck, Germany

ARTICLE INFO

Article history:
Received 3 June 2009
Revised 21 August 2009
Available online 1 October 2009

Keywords:
Double-wave-vector diffusion weighting
Tensor model
Diffusion anisotropy
Microscopic anisotropy
MA

ABSTRACT

Experiments with two diffusion-weighting periods applied successively in a single experiment, so-called double-wave-vector (DWV) diffusion-weighting experiments, are a promising tool for the investigation of material or tissue structure on a microscopic level, e.g. to determine cell or compartment sizes or to detect pore or cell anisotropy. However, the theoretical descriptions presented so far for experiments that aim to investigate the microscopic anisotropy with a long mixing time between the two diffusion weightings, are limited to certain wave vector orientations, specific pore shapes, and macroscopically isotropic samples. Here, the signal equations for fully restricted diffusion are re-investigated in more detail. A general description of the signal behavior for arbitrary wave vector directions, pore or cell shapes, and orientation distributions of the pores or cells is obtained that involves a fourth-order tensor approach. From these equations, a rotationally invariant measure of the microscopic anisotropy, termed MA, is derived that yields information complementary to that of the (macroscopic) anisotropy measures of standard diffusion-tensor acquisitions. Furthermore, the detailed angular modulation for arbitrary cell shapes with an isotropic orientation distribution is derived. Numerical simulations of the MR signal with a Monte-Carlo algorithms confirm the theoretical considerations. The extended theoretical description and the introduction of a reliable measure of the microscopic anisotropy may help to improve the applicability and reliability of corresponding experiments.

1. Introduction

Experiments where multiple diffusion-weighting periods are applied successively in a single acquisition were initially considered by Mitra [1] theoretically. First experiments were performed by Cory et al. [2] and Callaghan and Manz [3] to assess pore eccentricity and the correlation of spin motion in different directions, respectively.

To analyze the basic principles of such experiments, Mitra considered fully restricted diffusion in isolated pores with an isotropic orientation distribution for the case of (i) an infinitesimal and (ii) an infinite mixing time between the diffusion-weighting periods. Thereby, he focused on two diffusion-weighting periods in an experiment. Because for short gradient pulses a diffusion-weighting period is equivalent to a scatter event [4] that can be characterized by a wave vector, such experiments often are referred to as two- or double-wave-vector (DWV) diffusion-weighting experiments in contrast to standard, single-wave-vector experiments [5].

For a vanishing mixing time, Mitra found a cosine-shaped signal modulation when varying the angle between the two wave vectors with a maximum for the antiparallel orientation [1]. Thereby, the modulation amplitude increases with the effective pore or cell size which allows to estimate cell or compartment sizes. Experimental demonstrations of this effect have been reported for biological samples [6], extracted spinal cord [6,7], and in the human brain *in vivo* [8,9]. Signal equations [10] and numerical simulations [7,11] for simple pore shapes and finite timing parameters were presented recently as well as an extended theoretical framework for arbitrary orientation distributions and pore shapes involving a rank-2 tensor model [12]. Furthermore, it has been shown that applying multiple concatenations of the two wave vectors yields an increased modulation amplitude [13] which may help to improve the detectability and accuracy of the size estimation, in particular on whole-body MR systems with their limited gradient amplitudes.

For long mixing times, the signal is expected to differ between parallel and orthogonal wave vector orientations but, in contrast to the experiment with short mixing time, only for anisotropic pores or cells [1]. Thus, microscopic diffusion anisotropy can be detected in samples that macroscopically appear isotropic, e.g. because of an isotropic orientation distribution of the cells. This

* Corresponding author. Address: Institut für Systemische Neurowissenschaften, Geb. W34, Universitätsklinikum Hamburg-Eppendorf, Martinistrasse 52, 20246 Hamburg, Germany. Fax: +49 40 7410 59955.
E-mail address: j.finsterbusch@uke.uni-hamburg.de (J. Finsterbusch).

1090-7807/$ - see front matter © 2009 Elsevier Inc. All rights reserved.
doi:10.1016/j.jmr.2009.09.015

is of particular interest because standard single-wave-vector experiments fail to resolve this anisotropy. The microscopic anisotropy effect has been demonstrated experimentally in yeast cells [14], liquid crystals [15], plant tissues [16], the gray matter of monkey brain *in vitro* [17] and pig spinal cord *ex vivo* [18]. Recently, numerical simulations to investigate the influence of finite timing parameters have been presented [11].

The basic signal equation underlying the anisotropy effect were reported by Mitra [1]. He argued that the effect is of fourth order in the wave vector's amplitude without evaluating details. Cheng and Cory [14] calculated the signal for parallel and orthogonal wave vector orientations in a sample with isotropically oriented ellipsoids. They could conclude that the signal for orthogonal wave vector orientations is reduced compared to the parallel orientation. Recently, signal equation calculations [10,19] as well as numerical simulations [11] were performed for simple pore shapes and finite values of the timing parameters, like the mixing and diffusion time.

All these approaches either assume an isotropic orientation distribution or a specific shape of the pores or cells. Thus, they are of limited value in biological tissue where the cell shape is irregular or unknown and the orientation distribution may deviate from an isotropic one. In particular the latter problem hampers the applicability because in general the signal will not only depend on the relative angle between the two wave vectors but also on their absolute orientations with respect to the cells' orientation distribution. This could be solved by performing acquisitions with wave vectors covering the full angular range isotropically. However, this would also include the orthogonal wave vector orientation, i.e. for each orientation of the first wave vector the second one needs to sample a perpendicularly oriented circle, which would yield excessive acquisition times.

In this work, the basic signal equation of fully restricted diffusion provided by Mitra for DWV experiments with long mixing times [1] is re-investigated in detail. A general description of the signal involving a fourth-order tensor equation is derived that is valid for any orientation distribution and shape of the cells and arbitrary wave vector directions. From this result, a rotationally invariant measure of the microscopic anisotropy, termed *MA*, is derived that reliably describes the diffusion anisotropy on a microscopic scale, and yields information complementary to that of the anisotropy measures of standard, single-wave-vector diffusion-tensor experiments. It is defined on the basis of the elements of the fourth-order tensor of the signal equation and can be determined experimentally by a measurement with parallel and orthogonal wave vector orientations. Furthermore, an analytical expression for the signal modulation for an isotropic orientation distribution of the pores or cells is calculated. The validity of the theoretical considerations is confirmed with numerical simulations using a Monte-Carlo algorithm.

2. Theory

In this section, the basic equation provided by Mitra [1] is re-investigated in detail. First, the results of previous works derived for isotropic orientation distributions are shortly summarized (Section 2.1). The analytical calculations start with a Taylor expansion up to fourth order of the signal equation derived by Mitra [1] (Section 2.2). After re-writing this expression using the modified Voigt notation (Section 2.3), a tensor equation of the signal is obtained that is valid for arbitrary wave vector and pore orientation distributions and for any pore shape (Section 2.4). In the following sections, an invariant is derived from the tensor elements that can be determined experimentally with a few measurements with parallel and orthogonal wave vector orientations (Section 2.5). This invariant is shown to depend on the eccentricity or anisotropy of the pores and can be used to define a pore-size independent measure *MA* of the microscopic anisotropy (Section 2.6). In case of a single pore orientation, the *MA* is in line with anisotropy measures known from standard diffusion tensor imaging (Section 2.7). But for arbitrary orientation distributions, the *MA* still reflects the anisotropy property present on a microscopic, i.e. pore, level (Section 2.8) and, thus, yields information complementary to that of the standard diffusion tensor anisotropies (Section 2.9). Finally, the general signal expression for an isotropic orientation distribution that can be derived from the tensor equation is presented and its consistency with previously reported results is shown (Section 2.10).

2.1. Results of previous works

The NMR signal M observed in a DWV diffusion-weighting experiment (Fig. 1) with wave vectors $\mathbf{q_1}$ and $\mathbf{q_2}$ was first evaluated by Mitra [1]. He considered fully restricted diffusion in isolated pores or cells with an isotropic orientation distribution. Furthermore, he assumed that the pulse durations δ_i are short ($\delta_i \to 0$) and the diffusion times Δ_i are large compared to τ_D ($\Delta_i \gg \tau_D$) which is the time a spin typically needs to diffuse across a pore, i.e. $\tau_D = \frac{a^2}{2D}$ with the pore diameter a and the diffusion coefficient D. For the case that the mixing time τ_m between the two wave vectors is also large compared to τ_D ($\tau_m \gg \tau_D$), he obtained

$$M(\mathbf{q_1},\mathbf{q_2}) \propto \sum_{j=1}^{N} \left|\tilde{\rho}_j(\mathbf{q_1})\right|^2 \left|\tilde{\rho}_j(\mathbf{q_2})\right|^2 \tag{1}$$

where $\tilde{\rho}_j(\mathbf{q})$ is the Fourier transformation of the spin density distribution ρ_j in pore j

$$\tilde{\rho}_j(\mathbf{q}) = \int_{\text{pore } j} \rho_j(\mathbf{r}) e^{i\mathbf{q}\mathbf{r}}\, d\mathbf{r} \tag{2}$$

Mitra found that Eq. (1) bears an interesting feature [1]. For spherical pores or cells, the signal solely depends on the magnitude of the wave vectors but not on their orientations. In contrast, the signal observed for non-spherical, e.g. ellipsoidal, pores or cells depends on the relative angle θ between the two wave vectors $\mathbf{q_1}$ and $\mathbf{q_2}$ which arises because the product of both contributions in Eq. (1) is taken before the summation over all pores is performed. As a consequence, samples with spherical and non-spherical pores or cells can be distinguished with the DWV experiment although both samples would appear isotropic in a standard, single-wave-vector experiment. In other words, a DWV experiment with long mixing time is able to detect a diffusion anisotropy present on a microscopic level in a macroscopically isotropic sample.

The angular dependency of the signal for anisotropic pores is expected to appear in the fourth order of the wave vector amplitude q according to [1]. A detailed analysis for ellipsoidal pores was presented by Cheng and Cory who calculated the signals for parallel and orthogonal wave vector orientations ($q = q_1 = q_2$) and obtained [14]

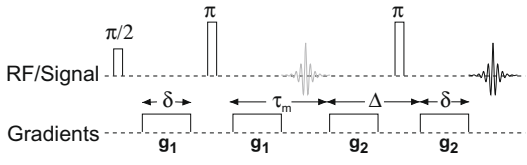

Fig. 1. Example of a basic pulse sequence for a double-wave-vector (DWV) diffusion-weighting experiment. It should be noted that the important feature, two diffusion-weighting periods applied successively in a single experiment, can be realized with various pulse sequences and is not limited to the double-spin–echo preparation shown here.

$$M_{||}(q) \propto 1 - c_2 q^2 + c_4 q^4$$
$$M_{\perp}(q) \propto 1 - d_2 q^2 + d_4 q^4 \tag{3}$$

with

$$c_2 = d_2 = \frac{4}{15}a^2 + \frac{2}{15}b^2$$
$$c_4 - d_4 = \frac{2}{375}\left(a^2 - b^2\right)^2 \tag{4}$$

where a and b are the semiaxes of the spheroidal pores.

In order to obtain a more general description of the signal, Eq. (1) needs to be re-investigated. A Taylor expansion is performed up to fourth order where the signal difference between parallel and orthogonal wave vector orientations appears for anisotropic pores.

2.2. Taylor expansion

Initially, an ensemble of identical pores or cells with a single orientation is considered which simplifies Eq. (1) to

$$M(\mathbf{q_1}, \mathbf{q_2}) \propto |\tilde{\rho}(\mathbf{q_1})|^2 |\tilde{\rho}(\mathbf{q_2})|^2 \tag{5}$$

where the pore index has been dropped for the sake of clarity. Because the expansion of Eq. (5) to fourth order can be composed of the terms obtained for the expansion of $\tilde{\rho}$ to the same order, $\tilde{\rho}$ will be considered first.

It is given by

$$\tilde{\rho}(\mathbf{q}) = 1 + i\mathbf{q}^T \int_{\text{pore}} \rho(\mathbf{r})\mathbf{r}\, d\mathbf{r} - \frac{1}{2}\sum_{j,k=1}^{3} q_j q_k \int_{\text{pore}} \rho(\mathbf{r}) r_j r_k\, d\mathbf{r} - \frac{i}{6}\sum_{j,k,l=1}^{3} q_j q_k q_l \int_{\text{pore}} \rho(\mathbf{r}) r_j r_k r_l\, d\mathbf{r} + \frac{1}{24}\sum_{j,k,l,m=1}^{3} q_j q_k q_l q_m \times \int_{\text{pore}} \rho(\mathbf{r}) r_j r_k r_l r_m\, d\mathbf{r} + \mathcal{O}(q^5) \tag{6}$$

where the pore or cell volume V has been set to $V = 1$ for simplicity. If the pore's center of gravity is chosen as the origin of the coordinate system the first order term vanishes and

$$\tilde{\rho}(\mathbf{q}) = 1 - \frac{1}{2}\sum_{j,k=1}^{3} q_j q_k \int_{\text{pore}} \rho(r) r_j r_k\, d\mathbf{r} - \frac{i}{6}\sum_{j,k,l=1}^{3} q_j q_k q_l \times \int_{\text{pore}} \rho(\mathbf{r}) r_j r_k r_l\, d\mathbf{r} + \frac{1}{24}\sum_{j,k,l,m=1}^{3} q_j q_k q_l q_m \times \int_{\text{pore}} \rho(\mathbf{r}) r_j r_k r_l r_m\, d\mathbf{r} + \mathcal{O}(q^5) \tag{7}$$

is obtained. Using the rank-2 (3×3) tensor $\underline{\underline{\mathbf{R}}}$ [12] and defining a rank-4 ($3 \times 3 \times 3 \times 3$) tensor $\underline{\underline{\underline{\underline{\mathbf{S}}}}}$ with elements

$$R_{jk} = \int_{\text{pore}} \rho(\mathbf{r}) r_j r_k\, d\mathbf{r}$$
$$S_{jklm} = \int_{\text{pore}} \rho(\mathbf{r}) r_j r_k r_l r_m\, d\mathbf{r} \tag{8}$$

Eq. (7) can be re-written to

$$\tilde{\rho}(\mathbf{q}) = 1 - \frac{1}{2}\mathbf{q}^T\underline{\underline{\mathbf{R}}}\mathbf{q} - \frac{i}{6}\sum_{j,k,l=1}^{3} q_j q_k q_l \int_{\text{pore}} \rho(\mathbf{r}) r_j r_k r_l\, d\mathbf{r} + \frac{1}{24} \times \sum_{j,k,l,m=1}^{3} q_j q_k q_l q_m S_{jklm} + \mathcal{O}(q^5) \tag{9}$$

Using these results, the Taylor expansion of $|\tilde{\rho}(\mathbf{q})|^2$ can be calculated to

$$|\tilde{\rho}(\mathbf{q})|^2 = \tilde{\rho}(\mathbf{q})\tilde{\rho}^*(\mathbf{q}) = 1 - \mathbf{q}^T\underline{\underline{\mathbf{R}}}\mathbf{q} + \frac{1}{4}(\mathbf{q}^T\underline{\underline{\mathbf{R}}}\mathbf{q})^2 + \frac{1}{12}\sum_{j,k,l,m=1}^{3} q_j q_k q_l q_m S_{jklm} + \mathcal{O}(q^6) \tag{10}$$

where the (imaginary) third order term of Eq. (9) has disappeared. Thus, the expansion of Eq. (5) up to fourth order yields

$$M(\mathbf{q_1}, \mathbf{q_2}) \propto 1 - \sum_{v=1}^{2} \mathbf{q}_v^T\underline{\underline{\mathbf{R}}}\mathbf{q}_v + \frac{1}{4}\sum_{v=1}^{2}\left(\mathbf{q}_v^T\underline{\underline{\mathbf{R}}}\mathbf{q}_v\right)^2 + \left(\mathbf{q}_1^T\underline{\underline{\mathbf{R}}}\mathbf{q}_1\right)\left(\mathbf{q}_2^T\underline{\underline{\mathbf{R}}}\mathbf{q}_2\right) + \frac{1}{12}\sum_{v=1}^{2} \times \sum_{j,k,l,m=1}^{3} q_{v,j} q_{v,k} q_{v,l} q_{v,m} S_{jklm} + \mathcal{O}(q^6) \tag{11}$$

where Greek and Latin indexes refer to the wave vector number and Cartesian coordinates, respectively, and $q_{v,j}$ is the jth component of wave vector $\mathbf{q}_v$. Beside the leading constant, Eq. (11) contains, in the order of appearance, (i) the second order term of $\tilde{\rho}$ and (ii) its square (fourth order) for each wave vector, (iii) a mixed product of the second order terms of $\tilde{\rho}$ between the two wave vectors (fourth order) that represents the interaction between the two wave vectors, and (iv) the fourth order term of $\tilde{\rho}$ for each wave vector.

Eq. (11) represents the desired general signal equation but is not very handy. However, it can be re-written into a more convenient expression using the modified Voigt notation.

2.3. Modified Voigt notation

The modified Voigt notation (also known as Voigt–Mandel notation) [20] will be used for the further investigations of Eq. (11). It allows to reduce the dimension of symmetric rank-4 tensors in order to yield a handier notation. For instance, a general rank-4 tensor has 81 elements but $\underline{\underline{\underline{\underline{\mathbf{S}}}}}$ whose elements S_{jklm} according to Eq. (8) are invariant under any permutation of the indices, has only 15 independent elements. It therefore can be expressed as a two-dimensional matrix in an appropriately chosen vector space.

Defining a six element vector $\tilde{\mathbf{q}}$ with

$$\tilde{\mathbf{q}} = \begin{pmatrix} q_1^2 \\ q_2^2 \\ q_3^2 \\ q_1 q_2 \\ q_1 q_3 \\ q_2 q_3 \end{pmatrix} \tag{12}$$

for each wave vector $\mathbf{q}_v$ allows to re-write the terms of the last sum in Eq. (11) according to

$$\frac{1}{12}\sum_{j,k,l,m=1}^{3} q_j q_k q_l q_m S_{jklm} = \frac{1}{12}\tilde{\mathbf{q}}^T\underline{\underline{\tilde{\mathbf{S}}}}\tilde{\mathbf{q}} \tag{13}$$

for each wave vector with

$$\underline{\underline{\tilde{\mathbf{S}}}} = \begin{pmatrix} S_{1111} & S_{1122} & S_{1133} & 2S_{1112} & 2S_{1113} & 2S_{1123} \\ S_{1122} & S_{2222} & S_{2233} & 2S_{1222} & 2S_{1223} & 2S_{2223} \\ S_{1133} & S_{2233} & S_{3333} & 2S_{1233} & 2S_{1333} & 2S_{2333} \\ 2S_{1112} & 2S_{1222} & 2S_{1233} & 4S_{1122} & 4S_{1123} & 4S_{1223} \\ 2S_{1113} & 2S_{1223} & 2S_{1333} & 4S_{1123} & 4S_{1133} & 4S_{1233} \\ 2S_{1123} & 2S_{2223} & 2S_{2333} & 4S_{1223} & 4S_{1233} & 4S_{2233} \end{pmatrix} \tag{14}$$

where a symmetric design was chosen and the factors reflect the multiplicity of the index combinations. Note that the position of

most elements is not unambiguously determined, only the elements S_{iiii} have a well-defined position within the matrix.

Analogously, the squares and the mixed product of the second order terms that contribute to the fourth order term, can be expressed as

$$\frac{1}{4}\left(\mathbf{q}^T\underline{\underline{\mathbf{R}}}\mathbf{q}\right)^2 = \frac{1}{4}\tilde{\mathbf{q}}^T\underline{\underline{\tilde{\mathbf{R}}}}\tilde{\mathbf{q}} \tag{15}$$

and

$$\left(\mathbf{q}_1^T\underline{\underline{\mathbf{R}}}\mathbf{q}_1\right)\left(\mathbf{q}_2^T\underline{\underline{\mathbf{R}}}\mathbf{q}_2\right) = \tilde{\mathbf{q}}_1^T\underline{\underline{\tilde{\mathbf{R}}}}\tilde{\mathbf{q}}_2, \tag{16}$$

respectively, with

$$\underline{\underline{\tilde{\mathbf{R}}}} = \begin{pmatrix} R_{11}^2 & R_{11}R_{22} & R_{11}R_{33} & 2R_{11}R_{12} & 2R_{11}R_{13} & 2R_{11}R_{23} \\ R_{11}R_{22} & R_{22}^2 & R_{22}R_{33} & 2R_{12}R_{22} & 2R_{13}R_{22} & 2R_{22}R_{23} \\ R_{11}R_{33} & R_{22}R_{33} & R_{33}^2 & 2R_{12}R_{33} & 2R_{13}R_{33} & 2R_{23}R_{33} \\ 2R_{11}R_{12} & 2R_{12}R_{22} & 2R_{12}R_{33} & 4R_{12}^2 & 4R_{12}R_{13} & 4R_{12}R_{23} \\ 2R_{11}R_{13} & 2R_{13}R_{22} & 2R_{13}R_{33} & 4R_{12}R_{13} & 4R_{13}^2 & 4R_{13}R_{23} \\ 2R_{11}R_{23} & 2R_{22}R_{23} & 2R_{23}R_{33} & 4R_{12}R_{23} & 4R_{13}R_{23} & 4R_{23}^2 \end{pmatrix}. \tag{17}$$

$\underline{\underline{\tilde{\mathbf{R}}}}$ has 21 different elements and, as $\underline{\underline{\tilde{\mathbf{S}}}}$, was set-up symmetrically. The elements are products of the six independent elements of $\underline{\underline{\mathbf{R}}}$ but it should be emphasized that this only holds for a single pore orientation as will be seen later.

Thus, Eq. (11) can be re-written to

$$M(\mathbf{q}_1,\mathbf{q}_2) \propto 1 - \sum_{v=1}^{2}\mathbf{q}_v^T\underline{\underline{\mathbf{R}}}\mathbf{q}_v + \frac{1}{4}\sum_{v=1}^{2}\tilde{\mathbf{q}}_v^T\underline{\underline{\tilde{\mathbf{R}}}}\tilde{\mathbf{q}}_v + \tilde{\mathbf{q}}_1^T\underline{\underline{\tilde{\mathbf{R}}}}\tilde{\mathbf{q}}_2 + \frac{1}{12} \times \sum_{v=1}^{2}\tilde{\mathbf{q}}_v^T\underline{\underline{\tilde{\mathbf{S}}}}\tilde{\mathbf{q}}_v \tag{18}$$

which, e.g. avoids rank-4 terms. A further simplification can be achieved when combining the two vectors $\mathbf{q}_v$ as well as the two vectors $\tilde{\mathbf{q}}_v$ as it is shown in the next section.

2.4. Tensor equation

Concatenating the $\mathbf{q}_v$ and the $\tilde{\mathbf{q}}_v$ vectors to single vectors $\mathbf{Q} = (\mathbf{q}_1^T,\mathbf{q}_2^T)^T$ and $\tilde{\mathbf{Q}} = (\tilde{\mathbf{q}}_1^T,\tilde{\mathbf{q}}_2^T)^T$, respectively, and using

$$\tilde{\mathbf{q}}_1^T\underline{\underline{\tilde{\mathbf{R}}}}\tilde{\mathbf{q}}_2 = \tilde{\mathbf{q}}_2^T\underline{\underline{\tilde{\mathbf{R}}}}\tilde{\mathbf{q}}_1 = \frac{1}{2}\left(\tilde{\mathbf{q}}_1^T\underline{\underline{\tilde{\mathbf{R}}}}\tilde{\mathbf{q}}_2 + \tilde{\mathbf{q}}_2^T\underline{\underline{\tilde{\mathbf{R}}}}\tilde{\mathbf{q}}_1\right) \tag{19}$$

yields the final tensor equation

$$M(\mathbf{Q}) \propto 1 - \frac{1}{2}\mathbf{Q}^T\underline{\underline{\mathbf{T}_a}}\mathbf{Q} + \frac{1}{12}\tilde{\mathbf{Q}}^T\underline{\underline{\tilde{\mathbf{U}}}}\tilde{\mathbf{Q}} \tag{20}$$

with the second order (6 × 6) tensor

$$\underline{\underline{\mathbf{T}_a}} = \begin{pmatrix} 2\underline{\underline{\mathbf{R}}} & 0 \\ 0 & 2\underline{\underline{\mathbf{R}}} \end{pmatrix} \tag{21}$$

and the fourth-order (12 × 12) tensor

$$\underline{\underline{\tilde{\mathbf{U}}}} = \begin{pmatrix} \underline{\underline{\tilde{\mathbf{S}}}} + 3\underline{\underline{\tilde{\mathbf{R}}}} & 6\underline{\underline{\tilde{\mathbf{R}}}} \\ 6\underline{\underline{\tilde{\mathbf{R}}}} & \underline{\underline{\tilde{\mathbf{S}}}} + 3\underline{\underline{\tilde{\mathbf{R}}}} \end{pmatrix} \tag{22}$$

respectively, which both are symmetric.

$\underline{\underline{\mathbf{T}_a}}$ can be seen in analogy to the tensor $\underline{\underline{\mathbf{T}}}$ that was introduced to describe the second order signal decay in DWV experiments with a vanishing mixing time [12] but, although it is based on the same six independent elements, has a slightly different definition.

With Eq. (20), a general expression for the MR signal in a DWV experiment with long mixing time has been derived that conveniently describes the signal for any wave vector direction and cell shape and that also holds for arbitrary orientation distributions of the cells as will be shown below. The off-diagonal $\underline{\underline{\tilde{\mathbf{R}}}}$ matrices that describe the mixed product of both wave vectors represent the interaction term that causes the modulation of the signal with the angle between the two wave vectors for anisotropic cells. This will also be seen in more detail later.

Although Eq. (20) is quite clear, it does not provide an apparent approach to estimate the pore anisotropy. A solution to this problem is presented in the following sections.

2.5. Rotational invariant and its experimental determination

In general, the signal described by Eq. (20) will not only depend on the relative angle between the two wave vectors but also on their absolute orientations relative to that of the pores. It is true that a signal difference between a parallel and an orthogonal orientation of the wave vectors indicates anisotropic cells. But the difference varies with the wave vector's absolute orientations and may even vanish, i.e. in case of equal signals for parallel and orthogonal wave vectors it must not be concluded that no microscopic anisotropy is present. Thus, this difference is not a reliable measure of the pore's anisotropy. This is very similar to standard diffusion-tensor acquisitions where from the difference of the diffusion coefficients in three orthogonal directions only a lower limit of the tensor's anisotropy can be estimated and all diffusion coefficients can be equal even in the presence of anisotropic diffusion.

A reliable measure of the cell or microscopic anisotropy, needs to (i) be based on the fourth order signal contributions, (ii) be rotationally invariant, (iii) be assessable by a limited number of acquisitions, i.e. wave vector orientation combinations, and should (iv) depend on the pores anisotropy or eccentricity but not on its size. These requirements are in line with the properties of diffusion-tensor anisotropy measures.

As a first approach, I_{MA} according to

$$I_{MA} = \frac{3}{2}\sum_{k=1}^{3}\tilde{R}_{kk} - \frac{1}{2}\sum_{k,l=1}^{3}\tilde{R}_{kl} + \frac{3}{4}\sum_{m=4}^{6}\tilde{R}_{mm} \tag{23}$$

is considered which due to the symmetry of $\underline{\underline{\tilde{\mathbf{R}}}}$ is equivalent to

$$I_{MA} = \sum_{k=1}^{3}\tilde{R}_{kk} - \sum_{\substack{k,l=1\\k<l}}^{3}\tilde{R}_{kl} + \frac{3}{4}\sum_{m=4}^{6}\tilde{R}_{mm} \tag{24}$$

i.e. involves nine different elements of $\underline{\underline{\tilde{\mathbf{R}}}}$.

Using the definition of $\underline{\underline{\tilde{\mathbf{R}}}}$ in Eq. (17) that was obtained for an ensemble of identical pores with a single orientation, it is identical to I_A given by

$$I_A = \sum_{k=1}^{3}R_{kk}^2 - \sum_{\substack{k,l=1\\k<l}}^{3}R_{kk}R_{ll} + 3\sum_{\substack{k,l=1\\k<l}}^{3}R_{kl}^2 \tag{25}$$

which is equivalent to

$$I_A = \left(\sum_{k=1}^{3}R_{kk}\right)^2 - 3\sum_{\substack{k,l=1\\k<l}}^{3}R_{kk}R_{ll} + 3\sum_{\substack{k,l=1\\k<l}}^{3}R_{kl}^2 = \mathrm{Tr}\left(\underline{\underline{\mathbf{R}}}\right)^2 - 3\sum_{\substack{k,l=1\\k<l}}^{3}\left(R_{kk}R_{ll} - R_{kl}^2\right). \tag{26}$$

Thus, I_A is the sum of the squared trace (invariant I_1) and a multiple of the surface element (invariant I_2) [21] of the tensor $\underline{\underline{\mathbf{R}}}$ [12] and as such is also rotationally invariant. This also holds for I_{MA}, so far strictly only for a single pore orientation, but it will be shown later that it is in general rotationally invariant, too.

I_{MA} can be determined from 15 diffusion-weighted measurements with different orientations of the two wave vectors, e.g. according to

$$I_{MA} = \sum_{k=1}^{3} M_{k,k} - \sum_{\substack{k,l=1 \\ k<l}}^{3} M_{k,l} + \frac{3}{2}\sum_{\substack{k,l=1 \\ k<l}}^{3}\left(\frac{1}{2}M_{kl,kl} + \frac{1}{2}M_{k\bar{l},k\bar{l}} - M_{kl,k\bar{l}}\right) \quad (27)$$

where $M_{k,l}$ is the signal obtained with the two wave vectors along the axes $\mathbf{e_k}$ and $\mathbf{e_l}$, and $M_{ij,kl}$ that obtained with the two wave vectors along the diagonals defined by $\mathbf{e_i}+\mathbf{e_j}$ and $\mathbf{e_k}+\mathbf{e_l}$. Thus, the 15 wave vector combinations of Eq. (27) cover (i) three parallel orientations along each axis plus (ii) four combinations in each kl-plane with (iia) two orthogonal and (iib) two parallel orientations ($3 \cdot 4 = 12$). For the xy-plane the "planar" orientations are given by (first $\oplus$ second wave vector) (iia) $(1,0,0)^T \oplus (0,1,0)^T$ and $(1,1,0)^T/\sqrt{2} \oplus (1,-1,0)^T/\sqrt{2}$, and (iib) $(1,1,0)^T/\sqrt{2} \oplus (1,1,0)^T/\sqrt{2}$ and $(1,-1,0)^T/\sqrt{2} \oplus (1,-1,0)^T/\sqrt{2}$. In the other two planes, the components must be permuted appropriately.

With the signal combination of Eq. (27), all elements of $\underline{\underline{\widetilde{\mathbf{S}}}}$ and those of $\underline{\underline{\widetilde{\mathbf{R}}}}$ that do not contribute to I_{MA} but in general appear in the signal of Eq. (20), are eliminated yielding only the desired expression of the fourth order terms according to Eq. (23). Furthermore, the constant and the second order terms of Eq. (20) vanish, too. Thus, a limited set of measurements is sufficient to determine I_{MA} experimentally.

It should be noted that the number of measurements is lower than the number of different elements of $\underline{\underline{\widetilde{\mathbf{U}}}}$, i.e. not all elements of $\underline{\underline{\widetilde{\mathbf{U}}}}$ need to be determined to obtain I_{MA}.

2.6. Microscopic anisotropy measures

From Eq. (25) it is seen that I_A vanishes for isotropic cells because in this case $R_{kk} = const$ and $R_{kl} = 0$ for $k \neq l$. This can also be seen in Eq. (27) as for isotropic cells all signals $M_{k,l}$ and $M_{ij,kl}$ are identical and appear equally weighted with positive and negative sign. Thereby, all positive signs refer to signals obtained with parallel wave vector orientations while all those with a negative sign correspond to orthogonal wave vector orientations. Because according to Mitra [1] and Cheng and Cory [14] a signal difference occurs between parallel and orthogonal wave vector orientations for anisotropic cells, I_A is expected to be sensitive to the cell anisotropy.

This is obvious if I_A is considered in the eigenvector coordinate system where $R_{kl} = 0$ for $k \neq l$ and $R_{kk} = R_k$ with the eigenvalues R_k. Eq. (25) then is equivalent to

$$I_A = \sum_{k=1}^{3} R_k^2 - \sum_{\substack{k,l=1 \\ k<l}}^{3} R_k R_l = \frac{1}{2}\sum_{\substack{k,l=1 \\ k<l}}^{3} (R_k - R_l)^2 \quad (28)$$

i.e. I_A is zero for isotropic cells ($R_k = R_l$) and positive if $R_k \neq R_l$ for any $k \neq l$ (anisotropic cells). For the example of a one-dimensional pore with length $2r$ that can be regarded as an ellipsoid with semiaxes of 0, 0, and r and represents the "most anisotropic" case, an I_A value of $\frac{1}{9}r^4$ is obtained.

I_A increases with the pore size for a given pore shape, e.g. multiplying all size parameters with a constant factor f yields an f^4-fold I_A. For a measure of the microscopic anisotropy, this size dependency is not desired and must be eliminated by an appropriate normalization. This can be achieved with the tensor $\underline{\underline{\mathbf{R}}}$ that describes the second order signal decay for each wave vector. Its elements can be obtained, for instance, using an appropriate wave vector orientation scheme (e.g. see the "tensor" scheme described below) or involving additional acquisitions with a different q value to separate second and fourth order contributions.

The simplest approach to a size measure is the (rotationally invariant) trace of $\underline{\underline{\mathbf{R}}}$ given by $\sum_k R_{kk}$ or $\sum_k R_k$, another invariant often used is $\sqrt{\sum_k R_k^2}$, the denominator in the definition of the fractional anisotropy [22]. Without loss of generality, the following considerations will focus on $\mathrm{Tr}(\underline{\underline{\mathbf{R}}})$ for the size normalization. But it should be kept in mind that other normalization approaches are possible and behave equivalently.

Thus, a dimensionless measure MA of the microscopic anisotropy can be defined as

$$MA := \sqrt{\frac{3}{2}\sum_{k=1}^{3}\widetilde{R}_{kk} - \frac{1}{2}\sum_{k,l=1}^{3}\widetilde{R}_{kl} + \frac{3}{4}\sum_{m=4}^{6}\widetilde{R}_{mm}}\Bigg/\sum_{k=1}^{3} R_{kk}$$
$$= \sqrt{\sum_{k=1}^{3}\widetilde{R}_{kk} - \sum_{\substack{k,l=1 \\ k<l}}^{3}\widetilde{R}_{kl} + \frac{3}{4}\sum_{m=4}^{6}\widetilde{R}_{mm}}\Bigg/\sum_{k=1}^{3} R_{kk}. \quad (29)$$

It is composed of the square root of I_{MA} which is sensitive to the microscopic anisotropy in the numerator and the trace of the tensor $\underline{\underline{\mathbf{R}}}$ which increases with the pore size and eliminates the size dependency present in I_{MA}. The square root in the numerator is applied to obtain a dimensionless measure.

For an ensemble of identical pores with a single orientation, Eqs. (25) and (28) are valid and MA is equivalent to the anisotropy A defined as

$$A = \sqrt{\sum_{k=1}^{3} R_{kk}^2 - \sum_{\substack{k,l=1 \\ k<l}}^{3} R_{kk}R_{ll} + 3\sum_{\substack{k,l=1 \\ k<l}}^{3} R_{kl}^2}\Bigg/\sum_{k=1}^{3} R_{kk} \quad (30)$$

and, in terms of the eigenvalues,

$$A = \sqrt{\frac{1}{2}\sum_{\substack{k,l=1 \\ k<l}}^{3}(R_k - R_l)^2}\Bigg/\sum_{k=1}^{3} R_k \quad (31)$$

respectively. For the example of ellipsoidal pores with semiaxes a, b, and c, Eq. (31) yields

$$A_{\mathrm{elli}} = \frac{\sqrt{\left(a^2-b^2\right)^2 + (a^2-c^2)^2 + \left(b^2-c^2\right)^2}}{\sqrt{2}\left(a^2+b^2+c^2\right)}. \quad (32)$$

This also shows that the MA value for an ellipsoid with semiaxes 0, 0, and r now is 1, independent of r.

For a single pore orientation there are parallels between the defined MA and anisotropy measures known from standard (single-wave-vector) diffusion tensor imaging that are considered in the next section.

2.7. Comparison with anisotropy measures of the diffusion tensor

Eq. (31) is equivalent to

$$A = \frac{\sqrt{\sum_k (R_k - \langle R\rangle)^2}}{\sqrt{6}\langle R\rangle} \quad (33)$$

with $\langle R\rangle = \frac{1}{3}\mathrm{Tr}(\underline{\underline{\mathbf{R}}}) = \frac{1}{3}\sum_k R_k$. This notation shows the similarity to the (macroscopic) anisotropy measure RA [22], the relative anisotropy, that is derived from the second order diffusion tensor according to

$$RA = \frac{\sqrt{\sum_k (D_k - \langle D\rangle)^2}}{\sqrt{6}\langle D\rangle} \quad (34)$$

with the eigenvalues of the diffusion tensor D_k and $\langle D\rangle = \frac{1}{3}\sum_k D_k$. Note that the diffusion coefficients D_k are proportional to the mean squared displacement, i.e. the elements of Eq. (34) can be re-written to be quadratic in r like those of Eq. (33).

A modified definition of the microscopic anisotropy measure that uses $\sqrt{\sum_k R_k^2}$ rather than $\sum_k R_k$ for the size normalization (as mentioned earlier)

$$A_F = A\frac{\sum_k R_{kk}}{\sqrt{\sum_k R_k^2}} \tag{35}$$

yields

$$A_F = \sqrt{\frac{3}{2}}\frac{\sqrt{\sum_k (R_k - \langle R\rangle)^2}}{\sqrt{\sum_k R_k^2}} \tag{36}$$

which corresponds to the diffusion tensor's fractional anisotropy [22]

$$FA = \sqrt{\frac{3}{2}}\frac{\sqrt{\sum_k (D_k - \langle D\rangle)^2}}{\sqrt{\sum_k D_k^2}}. \tag{37}$$

This means that $A_{(F)}$ which is identical to *MA* for the special case of a single pore orientation, can be considered as a measure of the macroscopic anisotropy.

However, two things should be emphasized. First, *RA* and *FA* refer to the diffusion tensor that can be considered to be equivalent to the *displacement* ellipsoid, while $A_{(F)}$ (and the *MA* measures) have been derived to estimate the *pore geometry* directly. Second, the *MA* measures represent a more general description of diffusion anisotropy because they reduce to $A_{(F)}$, and thus *RA*- and *FA*-like expressions, only if an ensemble of identical pores with a single orientation is considered as assumed for Eq. (30). In this case, the microscopic and macroscopic anisotropy are identical. However, for multiple ensembles $A_{(F)}$, and *RA* as well as *FA*, refer to the macroscopic anisotropy while *MA* characterizes the microscopic anisotropy. Thus, the values of the *MA* measures differ in general from those of $A_{(F)}$ (or *RA* and *FA*) and, for instance, do not vanish in samples with an isotropic orientation distribution of anisotropic cells as will be shown in the next sections.

2.8. Multiple pore ensembles

It could be argued that considering the fourth order signal contributions in Eq. (20) is not required in practice because all terms appearing in I_A according to Eq. (25) are derived from the tensor elements of $\underline{\underline{\mathbf{R}}}$ that describe the signal decay in the second order. This is true as long as only a single pore ensemble is assumed, as has been done for the derivation of Eq. (25), which also means that the macroscopic and the microscopic anisotropy are identical. Taking multiple pore ensembles, e.g. with different orientations, into account introduces a crucial difference between the second and fourth order signal contributions that causes the discrepancy between the microscopic and macroscopic anisotropy measures.

Assuming different ensembles, each with a relative weight of p_j ($\sum_j p_j = 1$), the signal of the pore mixture is obtained by adding up the contributions of the individual pore ensembles. This means that Eq. (20) remains valid if the weighted sums are used for the tensors involved, i.e.

$$\begin{aligned}\underline{\underline{\widetilde{\mathbf{T}}_{\mathbf{a}}}} &= \sum_j p_j \underline{\underline{\widetilde{\mathbf{T}}_{\mathbf{a}j}}}\\ \underline{\underline{\widetilde{\mathbf{U}}}} &= \sum_j p_j \underline{\underline{\widetilde{\mathbf{U}}_j}}\end{aligned} \tag{38}$$

and

$$\begin{aligned}\underline{\underline{\mathbf{R}}} &= \sum_j p_j \underline{\underline{\mathbf{R}}_j}\\ \underline{\underline{\widetilde{\mathbf{R}}}} &= \sum_j p_j \underline{\underline{\widetilde{\mathbf{R}}_j}}\\ \underline{\underline{\widetilde{\mathbf{S}}}} &= \sum_j p_j \underline{\underline{\widetilde{\mathbf{S}}_j}}\end{aligned} \tag{39}$$

where $\underline{\underline{\widetilde{\mathbf{T}}_{\mathbf{a}j}}}$, $\underline{\underline{\widetilde{\mathbf{U}}_j}}$, $\underline{\underline{\mathbf{R}}_j}$, $\underline{\underline{\widetilde{\mathbf{R}}_j}}$, and $\underline{\underline{\widetilde{\mathbf{S}}_j}}$ are the tensors for the individual ensembles. This also holds for the definitions of I_{MA} and *MA*, i.e. Eqs. (23), (24), and (29). Furthermore, because I_{MA} is linear in the elements of $\underline{\underline{\widetilde{\mathbf{R}}}}$,

$$I_{MA} = \sum_j p_j I_{MA,j} \tag{40}$$

and it can be concluded that I_{MA} as a sum of rotational invariants itself is also rotationally invariant in case of multiple pore ensembles.

Modeling the measured signal according to Eq. (20) now yields the averaged tensor elements

$$R_{kl} = \sum_j p_j R_{j,kl} \tag{41}$$

with $R_{j,kl}$ being the kl-element of $\underline{\underline{\mathbf{R}}_j}$ and, for $k, l < 4$,

$$\widetilde{R}_{kl} = \sum_j p_j \widetilde{R}_{j,kl} = \sum_j p_j R_{j,kk} R_{j,ll} \tag{42}$$

which yields the important difference between I_{MA} and I_A:

$$\widetilde{R}_{kl} = \sum_j p_j R_{j,kk} R_{j,ll} \neq \sum_j p_j R_{j,kk} \cdot \sum_j p_j R_{j,kk} = R_{kk} R_{ll} \tag{43}$$

For $\widetilde{R}_{kl}$, used in I_{MA}, the elements of the individual $\underline{\underline{\mathbf{R}}_j}$ are multiplied prior to averaging over multiple ensembles and, thus, cannot be obtained from the (averaged) R_{kl} (used for I_A) anymore as for a single pore ensemble. Consequently, the $\widetilde{R}_{kl}$ in general must be considered as independent variables. This is why the definition of the microscopic anisotropy measures is based on them (rather than on the R_{kl}) and in general differs from the macroscopic anisotropy measures.

This crucial difference can be demonstrated for a simple example of one-dimensional pores, i.e. ellipsoidal pores with semiaxes of 0, 0, and r and a constant spin density $\rho(\mathbf{r}) = \rho$. For a single ensemble ($p_1 = 1$) with pores oriented along x, the only element of $\underline{\underline{\mathbf{R}}}$ that does not vanish is $R_{11} = \frac{1}{3}r^2$. This yields a *MA* of $\sqrt{\frac{1}{9}r^4}/(\frac{1}{3}r^2) = 1$ that is identical to the macroscopic value (A). Considering two ensembles oriented along x and y with identical weighting factors $p_j = \frac{1}{2}$, yields the same value for *MA* $\sqrt{2\cdot\frac{1}{2}\frac{1}{9}r^4}/(\frac{1}{3}r^2) = 1$ but because $R_{11} = R_{22} = \frac{1}{6}r^2$, A yields $\sqrt{2\cdot\frac{1}{36}r^4 - \frac{1}{36}r^4}/(\frac{1}{3}r^2) = \frac{1}{2}$, i.e. half the value. Adding a third ensemble along z ($p_j = \frac{1}{3}$) also does not change *MA* because $\sqrt{3\cdot\frac{1}{3}\frac{1}{9}r^4}/(\frac{1}{3}r^2) = 1$. But because now $R_{11} = R_{22} = R_{33} = \frac{1}{9}r^2$, the macroscopic anisotropy A vanishes: $\sqrt{3\cdot\frac{1}{81}r^4 - 3\cdot\frac{1}{81}r^4}/(\frac{1}{3}r^2) = 0$.

2.9. Microscopic and macroscopic anisotropy

The anisotropy A defined according to Eq. (30) in general represents a measure of the macroscopic anisotropy that can be calculated from the elements of the second order tensor $\underline{\underline{\mathbf{R}}}$. Thus, the macroscopic anisotropy A and the microscopic anisotropy *MA* can be determined from the same DWV experiment. This is interesting as they describe diffusion anisotropy on different length scales (cell vs. voxel scale), i.e. they consider complementary aspects of the diffusion anisotropy. Their comparison therefore yields additional information on the sample's structure.

The macroscopic anisotropy describes the direction preference of the diffusion averaged over the voxel. But, for instance, it does not distinguish between densely packed cells with an almost isotropic orientation distribution and a low density of anisotropic cells with a single orientation. Thus, the reason for a reduced macroscopic anisotropy could be a lower density of anisotropic cells or a more incoherent orientation of the cells. The microscopic anisotropy reflects the cell geometry but is independent from the cell's orientation distribution. Thus, it depends on the density of anisotropic cells but not on their orientation coherence on the voxel level.

Combining the information of both anisotropy measures allows to detect and distinguish between a reduced orientation coherence or a reduced density of anisotropic cells. This can, for instance, be achieved by simply considering the ratio of the anisotropy measures *RA*/*MA* (if *RA* is the preferred measure of the macroscopic anisotropy). It represents the "macroscopicity" of the diffusion anisotropy, i.e. the fraction of the anisotropy present on a microscopic scale that is also visible on the voxel scale. This reflects the degree of coherence of the orientation of the anisotropic pores. It yields 1 for a single cell orientation and 0 for an isotropic one. Similarly, a "microscopicity" could be defined as $1 - RA/MA$ that describes the degree of diffusion anisotropy present on a microscopic level but hidden on a macroscopic scale due to a (partially) incoherent orientation of the cells.

2.10. Isotropic orientation distribution

As a special case of multiple pore ensembles, an isotropic orientation distribution of identical cells will now be considered. Previous studies reported a signal difference between parallel and orthogonal wave vectors in this case for ellipsoidal cells [1,14] but so far, no general expression has been presented that (i) describes the dependency of the signal on the angle between the two wave vectors or (ii) the modulation amplitude for a general cell shape. Thus, the results of the previous sections were considered for an isotropic orientation distribution in order to derive such a general expression (see Appendix).

The signal equation obtained for $q_1 = q_2 = q$ is given by

$$M_{\mathrm{iso}}(q,\theta) \propto 1 - \frac{2}{3}\langle R^2\rangle q^2 + \left[\frac{1}{30}\left(3\langle R^4\rangle + 3\langle R_{kk}R_{ll}\rangle + 4\langle R_{kl}^2\rangle\right) + \frac{1}{15}\langle R_{kl}^2\rangle \cos 2\theta\right] q^4 \tag{44}$$

The signal modulation with the angle between the two wave vectors originates from the off-diagonal $\underline{\underline{\tilde{\mathbf{R}}}}$ matrices and is described by $\cos 2\theta$ which yields the difference between parallel and orthogonal wave vector orientations. The amplitude of the modulation is proportional to $\langle R_{kl}^2\rangle$ or $\langle R_{kk}^2\rangle - \langle R_{kk}R_{ll}\rangle$, i.e. to the square of the *MA* given by (see Appendix)

$$MA \propto \sqrt{\langle R_{kl}^2\rangle} = \sqrt{\frac{1}{2}\left(\langle R_{kk}^2\rangle - \langle R_{kk}R_{ll}\rangle\right)} \tag{45}$$

It vanishes for isotropic cells where $R_{kk} = R_{ll}$ for arbitrary k and l and $\langle R_{kl}^2\rangle$ is 0.

Considering the special case of ellipsoidal pores with semiaxes of a, a, and b and

$$R_{aa} = \frac{1}{5}a^2, \quad R_{bb} = \frac{1}{5}b^2 \tag{46}$$

yields

$$\frac{2}{3}\langle R^2\rangle = \frac{2}{3}(2R_{aa} + R_{bb}) = \frac{4}{15}a^2 + \frac{2}{15}b^2 \tag{47}$$

for the second order term and

$$\begin{aligned}\frac{1}{15}\langle R_{kl}^2\rangle &= \frac{1}{15}\left(\sum_k R_{kk}^2 - \sum_{k,l|k<l} R_{kk}R_{ll}\right)\\ &= \frac{1}{15}\left(2R_{aa} + R_{bb} - R_{aa}^2 - 2R_{aa}R_{bb}\right) = \frac{1}{15}(R_{aa} - R_{bb})^2\\ &= \frac{1}{375}(a^2 - b^2)^2\end{aligned} \tag{48}$$

for the modulation amplitude which corresponds to a signal difference between parallel and orthogonal wave vector orientations of

$$M_{\mathrm{iso}}(q,0) - M_{\mathrm{iso}}\left(q,\frac{\pi}{2}\right) = \frac{2}{375}(a^2 - b^2)^2 \tag{49}$$

and is consistent with Eq. (4) derived by Cheng and Cory.

3. Experimental

To evaluate the presented tensor approach and the microscopic anisotropy measure derived from it, Monte-Carlo simulations were performed. A self-written IDL algorithm (version 7.0, ITT Visual Information Solutions, Boulder, USA) described in more detail in [12] was used to simulate fully restricted diffusion of spins in isolated pores, calculate their averaged signal present in a DWV experiment, and analyze it with respect to the signal equation and the *MA* according to Eq. (20) and Eq. (29), respectively. For each spin a random starting point within the pore was determined and for every time unit a random, Gaussian displacement in a random direction was accumulated. At the pore boundaries, diffuse reflection was assumed. Identical wave vector amplitudes were used for both wave vectors ($q_1 = q_2$) for all simulations. Relaxation effects were neglected.

A pool of 10,000 spins was investigated with a time unit of dt = 1 μs. To approach the assumptions underlying the theoretical considerations, i.e. $\delta \to 0$ and $\tau_m, \Delta \gg \tau_D$ for the diffusion coefficient used ($2.0 \cdot 10^{-3}$ mm^2 s^{-1}), a gradient pulse length of one time unit and mixing times τ_m and diffusion times Δ of 40 ms were used. For pores with radii of 1.5, 2.0, and 2.5 μm, τ_m/τ_D and Δ/τ_D then are about 53.3, 30.0, and 19.2, respectively.

Different direction schemes were used for the orientations of the two wave vectors to investigate the different aspects of the theoretical considerations. As the simplest approach, the so-called "circle" scheme was applied in order to (i) demonstrate the variability of signal modulations with the angle between the two wave vectors that can be present in samples with non-isotropic orientation distribution, and (ii) confirm the feasibility of Eq. (20) to describe all modulation curves observed consistently. Thereby, the direction of one of the two wave vectors was fixed while the other one uniformly sampled a circle within a given plane that includes the first wave vector, with 72 directions. A Levenberg–Marquardt algorithm was applied to fit the individual data sets to Eq. (20) independently and estimate the pore parameters within the circle plane.

In the so-called "isotropic" direction scheme the directions of both wave vectors were uniformly distributed over a sphere. For each wave vector, 36 circles of latitude were defined in steps of 5°. On each circle, equidistant directions were defined with the number of directions on a circle being proportional to its circumference and a maximum number of 72 on the equator (corresponding to a separation of 5°). This approach yields a total number of 1651 directions for the first wave vector. For the second wave vector, these directions plus their antipodes were used, i.e. in total 1651 × 3302 = 5,451,602 combinations were applied.

The intention of this direction scheme was twofold. First, averaging all signals obtained with the same angle θ enclosed by any of the first and any of the second wave vectors yields the (orientation-independent) signal obtained for an isotropic orientation

distribution as pointed out earlier [12]. Thus, the validity of Eq. (44) can be checked. In the averaging step, θ was rounded to multiples of 5° to ensure that the averaging was performed over a sufficiently large range of different absolute wave vector orientations. Second, every combination simulated can be considered as an individual experiment for the given absolute wave vector orientations. Thus, Eq. (20) can be fitted to all simulation results testing the performance of this equation to describe the simulated signals over a large range of orientations with a single set of $\underline{\underline{\mathbf{R}}}$ and $\underline{\underline{\underline{\mathbf{U}}}}$, i.e. $\underline{\underline{\widetilde{\mathbf{R}}}}$ and $\underline{\underline{\widetilde{\mathbf{S}}}}$. For both approaches, a Levenberg–Marquardt algorithm was used to fit the underlying equations.

Because Eq. (20) aims to describe the signal to fourth order with in general 42 parameters, six of them for the second order, 36 for the fourth order, a reduced direction scheme, the so-called "tensor" scheme was applied. It is based on the nine directions used in Eq. (27), i.e. three directions along the axes and six non-collinear diagonals within the three coordinate planes, and involves the 45 different combinations obtained when neglecting the order of the directions in the combination. These combinations are expected to be sufficient to derive the full tensor information. The simulated signals were fitted to Eq. (20) using a Levenberg–Marquardt algorithm to obtain all tensor elements.

Furthermore, a so-called "anisotropy" direction scheme was used consisting of the 15 direction combinations of Eq. (27). This scheme represents a subset of the tensor scheme and has the minimum number of directions to calculate *MA* if the pore size is known. From the corresponding simulations, *MA* can be calculated analytically. One thousand two hundred rotations of this scheme were generated by applying random azimuthal and longitudinal rotation angles and were investigated to demonstrate the rotational invariance of *MA*.

In general, the fits to Eq. (20) were based on the general expression involving multiple pore ensembles, i.e. the $\widetilde{R}_{kl}$ were assumed to be independent of the R_{kl}. This case will be referred to as the general tensor equation and yields 42 independent variables, six in the second order and 36 in the fourth order contributions of Eq. (20), 15 of $\underline{\underline{\widetilde{\mathbf{S}}}}$ and 21 of $\underline{\underline{\underline{\underline{\widetilde{\mathbf{R}}}}}}$. In the corresponding fits, the boundary condition $\widetilde{R}_{kl} \geqslant 0$ for $k, l \leqslant 3$ was used that is a consequence of $R_{kk} \geqslant 0$ and $R_{kl}^2 \geqslant 0$. For some fits to simulations with a single pore ensemble, the simplified tensor equation was used where the $\widetilde{R}_{kl}$ were defined by the elements of $\underline{\underline{\mathbf{R}}}$ according to Eq. (17) yielding only 21 parameters, six elements R_{kl}, present in the second ($\underline{\underline{\mathbf{R}}}$) and fourth order ($\underline{\underline{\underline{\underline{\widetilde{\mathbf{R}}}}}}$), and the 15 different elements of $\underline{\underline{\widetilde{\mathbf{S}}}}$.

The deviations of the pore-size parameters or tensor elements that were determined from the fits, from their nominal values that can be calculated analytically, are given as a percentage. For those parameters or elements that have a nominal value of zero, the percentage is given relative to the non-vanishing nominal parameter or element with the lowest absolute value.

4. Results

In Fig. 2, the simulation results for the circle direction scheme applied in several circle planes and with different directions of the first wave vector are shown. As references, curves obtained for spherical pores (triangles) with radii between 1.5 and 2.5 μm are included. Some minor signal variations with θ, the angle between the two wave vectors, are visible for the spherical pores that similarly have been observed earlier [12] and may be caused by rounding errors or the hidden algorithm of the random number generator. For the large spherical pores, this modulation is slightly reduced if a longer τ_m is used (data not shown). However, because the modulations are neglectable, the τ_m used in the presented simulations was used throughout the manuscript in order to avoid excessive simulation times.

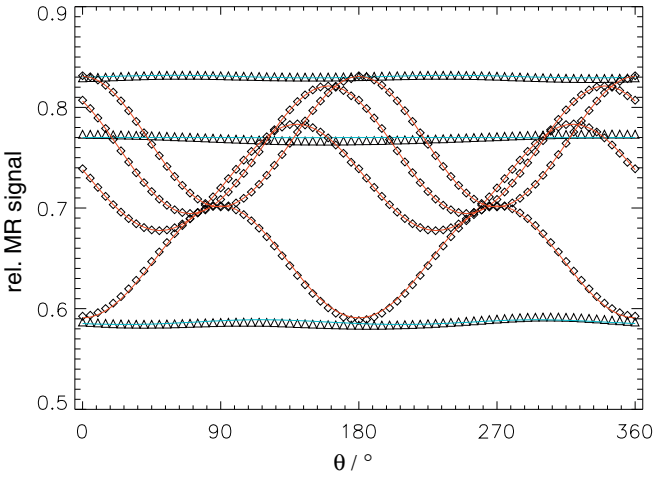

Fig. 2. Simulated MR signals (symbols) and corresponding fits to the tensor equation (solid lines) vs. the angle θ between the two wave vectors for the circle direction scheme where one wave vector is fixed and the other samples a circle. The simulations were performed for spherical pores (triangles) with radii of 1.5, 1.8, and 2.5 μm and parallel oriented ellipsoidal pores (diamonds) with semiaxes of 1.5, 1.5, and 2.5 μm. Several circle planes with different orientations of the first wave vector were simulated for the ellipsoidal pores. A single pore orientation was assumed for the fits.

For ellipsoidal cells (semiaxes 1.5, 1.5, and 2.5 μm) with a single pore orientation the signal curves (diamonds) show pronounced modulations with θ. Some plots show a minimum signal for the orthogonal wave vector orientation as expected for the anisotropy effect, however, others have an intermediate value or even a maximum at an angle of 90° between the two wave vectors. This is due to the fact that the signal amplitude for a single pore orientation strongly depends on the orientation of the two wave vectors relative to the pores yielding a variety of modulation amplitudes and phases. This holds for any other non-isotropic orientation distribution of anisotropic pores. As a consequence, two acquisitions with parallel and orthogonal wave vector orientations will commonly fail to determine the (microscopic) anisotropy reliably in the case of non-isotropic orientation distributions and a more general approach is required.

The fits to the simplified tensor equation in the circle plane (lines) are in good agreement with the simulations, the corresponding pore-size parameters are within 1% and 5% of the nominal values for the spherical and ellipsoidal pores, respectively. Thereby, a slight, but systematic underestimation is observed for the ellipsoidal pores that has also been reported in previous studies [12] and that was observed in most of the simulations performed in this work. Most likely, these deviations are due to higher order signal contributions that are not considered in the theoretical considerations. However, the pore eccentricity, i.e. the ratio of the long and short semiaxis, derived from the estimated diameters in the circle planes could be determined with an accuracy of about 1%.

In Fig. 3, a subset of the simulation data obtained with the isotropic direction scheme for parallel oriented ellipsoidal pore is presented. Each data point (diamond) represents the signal observed for a certain orientation combination of the two wave vectors relative to the orientation of the ellipsoidal pore. Although only a minor part of the data points is shown in Fig. 3, the fits (lines) to Eq. (20) were based on all (about 5.4 million) data points using a single parameter set. Thereby, the fit was performed either (i) under the assumption of a single pore ensemble orientation, i.e. with the 21 different parameters of $\underline{\underline{\mathbf{R}}}$ and $\underline{\underline{\widetilde{\mathbf{S}}}}$ and the elements of $\underline{\underline{\underline{\underline{\widetilde{\mathbf{R}}}}}}$ being derived from the R_{kl} according to Eq. (17) (Fig. 3a), or (ii) for the general case that takes multiple pore orientations into account

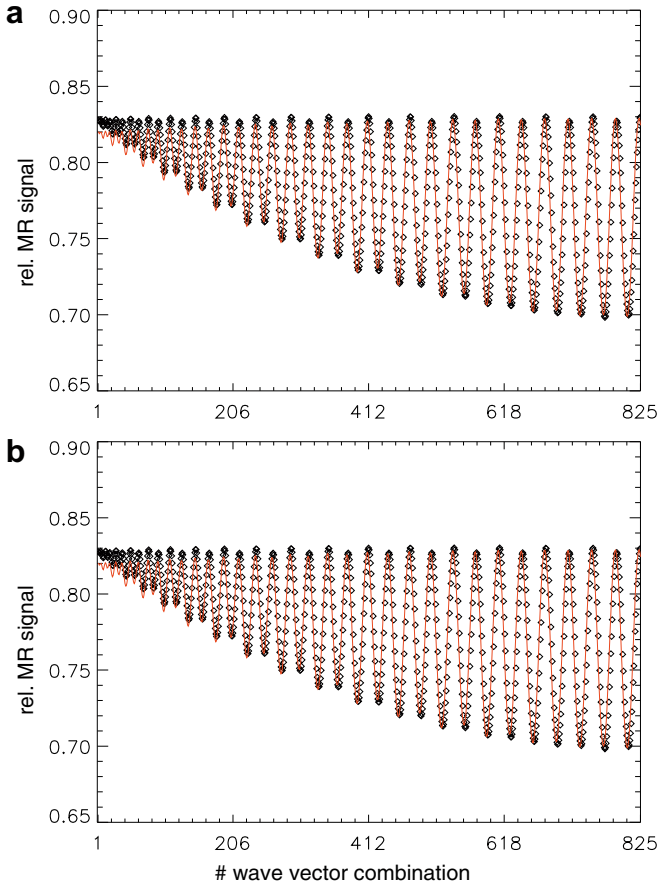

Fig. 3. Simulated MR signal (diamonds) and fits to the tensor equation (solid lines) for a subset covering 825 wave vector combinations (x axis) of the isotropic direction scheme for parallel oriented ellipsoidal pores with semiaxes of 1.5, 1.5, and 2.5 μm. Each data point represents the signal obtained for a certain combination of the wave vector orientations. The solid line represents the fit to all (more than 5.4 million) combinations investigated to Eq. (20) either (a) assuming a single pore orientation or (b) taking multiple pore orientations into account. For details see text.

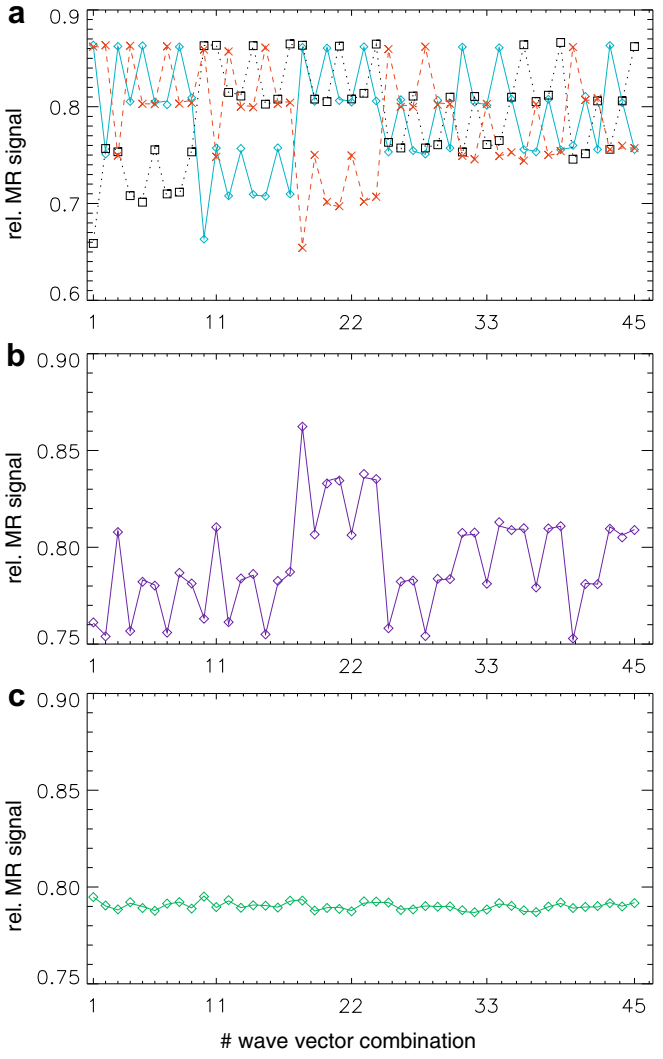

Fig. 4. Simulated MR signal (symbols) and fit to the tensor equation (lines) for the tensor direction scheme covering 45 orientation combinations of the wave vectors (x axis) and ellipsoidal pores with semiaxes of 1.5, 1.5, and 2.5 μm. In (a), three individual pore orientations (major semiaxis along x, y, or z) are shown, in (b) and (c) equally weighted mixtures of pores with orientations along (b) two (x,y) or (c) three orthogonal directions (x,y,z).

by using $\widetilde{R}_{kl}$ as independent variables yielding 21 additional parameters, i.e. 42 in total (Fig. 3b). Both fits approximate the simulated data very well and the underlying pore-size parameters are in a good agreement with the nominal values with a maximum deviation of about 5%. This demonstrates the feasibility of the derived tensor equation to describe the signal for arbitrary pore and wave vector orientations accurately even in the general case that takes multiple pore orientations into account.

Because the signal behavior described by Eq. (20) in the general case of multiple pore orientations (i.e. independent $\widetilde{R}_{kl}$) is based on 42 different parameters, the tensor direction scheme covering 45 wave vector orientation combinations is expected to be sufficient to determine all parameters describing the signal behavior. Simulation results (symbols) for this scheme and ellipsoidal cells are shown in Fig. 4 together with the fits to the tensor equation (solid lines). In Fig. 4a, the results for three different orientations of the pores, major semiaxis along x, y, and z, respectively, are presented. Because with only nine different directions the sampling of the wave vector orientations is quite sparse, the signal amplitudes accumulate at a few different signal "levels". As expected, the data values seem to be identical for the different pore orientations but appear at different wave vector orientations (see e.g. the minimum signal value below 0.6). The large variations of the signal amplitude are again due to the dependency of the signal amplitude on the wave vector orientation relative to the pore orientation. The fits to the general tensor equation (with 42 parameters) are in good agreement with the simulated data and yield pore parameters that differ by less than 1% between the different pore orientations and are within 5% of the nominal values.

For Fig. 4b, a mixture of two of the pore orientations (along x and y) with identical weightings was simulated. The modulation amplitude is reduced but the fit to the general tensor equation is again in good agreement with the simulated data and the fit parameters are within 5% of the nominal values of the ensemble mixture. This also holds for Fig. 4c, where a mixture of all three orientations (x, y, and z) is considered and the signal variation with the wave vector orientations is further reduced. Thus, it is demonstrated that (i) the general tensor equation is also a good model for the signal in the presence of multiple pore orientations and (ii) its parameters can be estimated reliably from a reasonable and realizable number of wave vector orientation combinations, e.g. the 45 of the tensor direction scheme.

Fig. 5 shows simulations for ellipsoidal pores with the anisotropy direction scheme, i.e. the 15 direction combinations used in Eq. (27). These combinations represent a minimum direction set

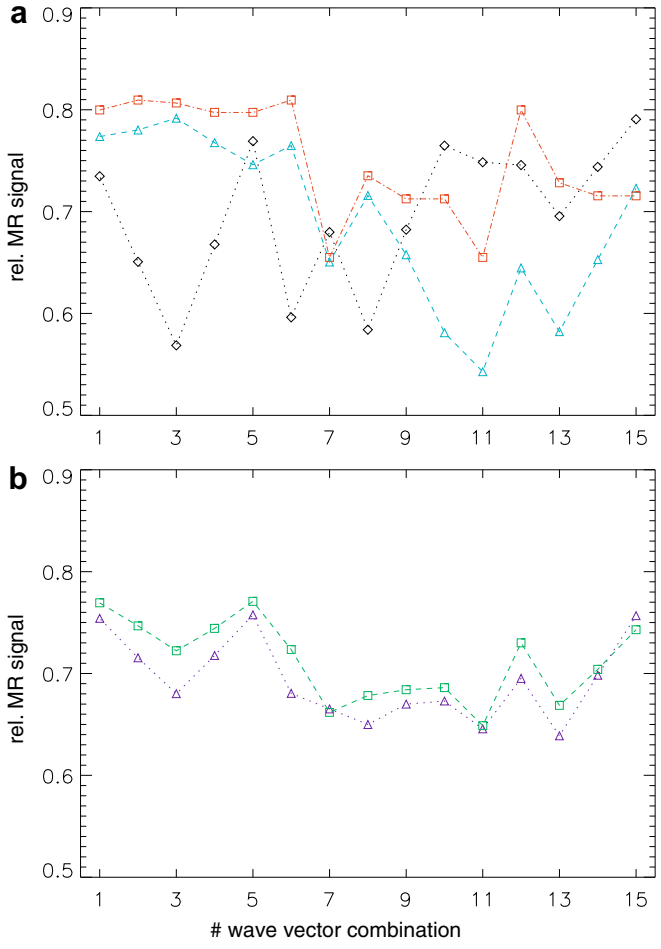

Fig. 5. Simulated MR signals in ellipsoidal pores (semiaxes 1.5, 1.5, 2.5 μm) for the wave vector orientations of the anisotropy direction scheme (*x* axis) and (a) single pore orientations along three different directions and (b) equally weighted mixtures of two (triangles) or three (squares) of these orientations.

required to determine a rotationally invariant measure of the pore anisotropy (I_{MA}). To calculate the size-independent *MA* a correction for the pore size is required. In order to focus to the essential property of *MA*, the description of the pore anisotropy, the nominal values of the pore size were used in this and the following calculations but it should be kept in mind that this information usually needs to be obtained experimentally as well.

In the different simulations presented in Fig. 5, the anisotropy scheme was applied to ellipsoidal pores with different pore orientations, three simulations with random single pore orientations (Fig. 5a) and two with a mixture of two or three of these directions (Fig. 5b). The signal range covered differs between the simulations with single pore orientations. One data set (diamonds) exhibits in general higher signal amplitude with a minimum signal amplitude of about $0.655\,M_0$ while the other two yield minimum values of about $0.55M_0$. However, the *MA* values calculated for these different data sets (0.376, 0.377, and 0.379, respectively) are very similar to the nominal value of $\frac{16}{43} \approx 0.372$, i.e. the maximum deviation is below 2%.

For the mixtures (Fig. 5b), the signal variations are decreased as their macroscopic anisotropy is reduced but the *MA* values obtained from the simulations are very similar to those of the single pore orientations (0.351 and 0.378, respectively) and within 6% and 2% of the nominal value, respectively. This indicates that, as expected from the theoretical considerations, the *MA* seems to be a reasonable parameter to characterize the pore anisotropy even in sample with non-isotropic orientation distributions and offers information beyond that of macroscopic anisotropy measures.

To confirm the rotational invariance of the *MA*, simulations with the anisotropy direction scheme were repeated for 1200 random, single pore orientations and using three different eccentricities of the ellipsoidal pores. The *MA* values obtained for the first 300 orientations are plotted in Fig. 6. Only minor variations of the *MA* values are observed that occur for a limited number of pore orientations. All values are within 4% of the nominal values (0.372, 0.327, and 0.263, respectively) and the mean values of all 1200 directions differ only by about 2.6% from the nominal values (lines). Thus, the rotational invariance of the *MA* can be considered to be confirmed.

In Fig. 7, I_A values calculated from simulations with the anisotropy direction scheme (symbols) are shown for ellipsoidal pores with three different effective sizes and various eccentricities. Thereby, one semiaxis was shortened while the other two were

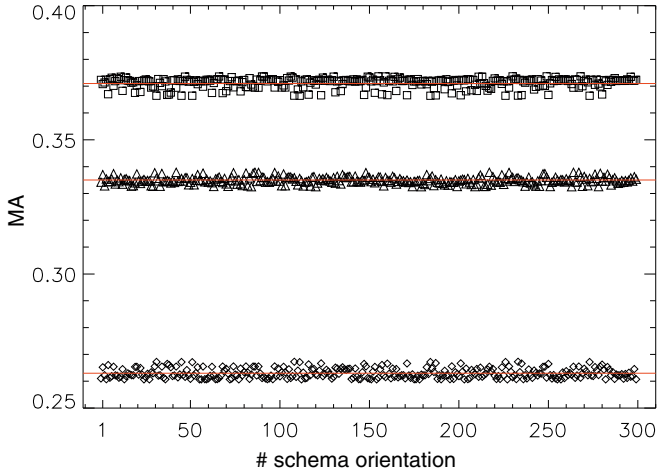

Fig. 6. *MA* values determined from simulations with the anisotropy direction scheme for parallel oriented ellipsoidal pores at the first 300 of 1200 different, randomly chosen absolute orientations (*x* axis). Three different pore geometries are shown with identical short semiaxes (1.5 and 1.5 μm) but different long semiaxis of 2.5 (squares), 2.35 (triangles), and 2.15 μm (diamonds) yielding nominal *MA* values of about 0.371, 0.335, and 0.263 (lines), respectively. For details see text.

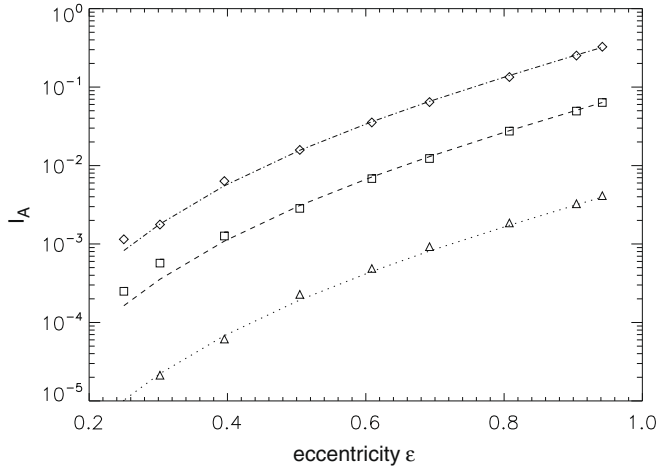

Fig. 7. Values of I_A calculated from simulations with the anisotropy direction scheme (symbols) for ellipsoidal pores with three different effective sizes and various eccentricities. Thereby, one semiaxis was shortened while the other two were prolonged such that $\langle R^2 \rangle$ remains constant (1.35 μm^2, 0.60 μm^2 and 0.15 μm^2, respectively). The theoretical curves are shown for comparison (dotted lines).

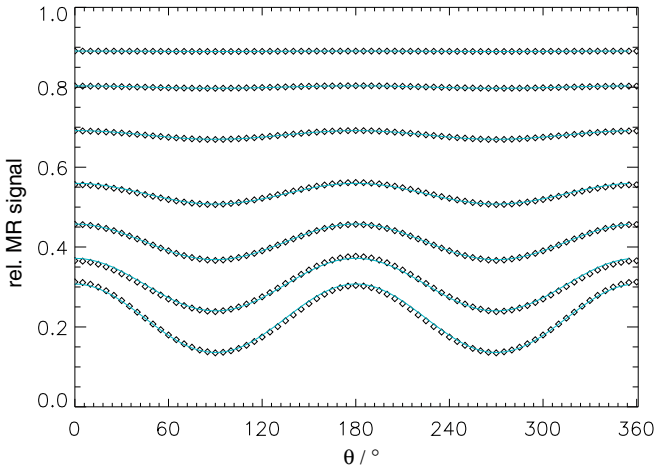

Fig. 8. Simulated MR signal (diamonds) vs. the angle θ between the two wave vectors for an isotropic orientation distribution of ellipsoidal pores with fixed short semiaxes (1.5 and 1.5 μm) and a variable long semiaxis ranging from 1.5 to 7.5 μm (top to bottom). The lines reflect the fits of the simulated data to the theoretical result.

prolonged such that the effective size as measured by $\langle R^2 \rangle$ remains constant. This means that any variation of the I_A is related to the change of the pore eccentricity. In any case, the pore eccentricity is given by $\epsilon = \sqrt{1 - a^2/b^2}$ where a and b are the short and long semiaxes, respectively. The data are in good agreement with the theoretical curve (dotted lines). Some deviations are observed for low eccentricities but it should be noted that the absolute deviations are small (typically below 0.005) and an ϵ of 0.25 represents almost isotropic pores with a difference between the long and short semiaxes of only 3.2%. Thus, it is shown that the I_A, and thus the *MA*, can be derived for a large spectrum of pores and clearly is attributed to the anisotropy effect.

Finally, an isotropic orientation distribution of ellipsoidal pores was simulated (Fig. 8) in order to confirm Eq. (44). Again ellipsoidal pores with different eccentricities were investigated. Increasing the long semiaxis, yields a lower signal due to the increased pore size but also a larger signal modulation amplitude which both is consistent with the theory. The fits agree well with the simulated data for the various eccentricities and their parameters deviate by less than 5% from the nominal values.

5. Discussion

The signal equation presented by Mitra [1] for a DWV experiment with a long mixing time has been evaluated in more detail yielding a tensor equation in the fourth order of the wave vector amplitude q. It describes the signal amplitude depending on the two wave vectors for arbitrary cell shapes and orientation distributions with, in general, 42 variables, six in the second order and 36 in the fourth order. From this equation, an analytical expression of the signal for an isotropic orientation distribution could be derived. Based on these theoretical results, rotationally invariant measures *MA* of the microscopic anisotropy were defined. In contrast to anisotropy measures derived from standard, single wave vector experiments, these measures reflect the pore geometry independently of the present orientation distribution, i.e. also for macroscopically isotropic samples. The major expression used for the definition of the *MA* measures can be obtained from 15 measurements with different wave vector orientations covering parallel and orthogonal alignments. However, to obtain values that solely depend on the pore eccentricity, a correction for the pore size must be performed. The signal curves obtained from numerical simulations of diffusion in ellipsoidal pores were in good agreement with the theoretical expectations. This also holds for the pore and *MA* parameters derived from fits of the analytical expressions to the simulated signal with a typical deviation of 5% or below.

It should be emphasized that the proposed direction scheme to determine the *MA* measures is a first approach that neither is expected to represent the only solution possible nor to be the optimal solution in terms of insensitivity to noise or gradient pulse durations required for the realization of the desired q values. However, regarding the long record on direction schemes for standard diffusion tensor acquisitions, an optimization for DWV experiments is beyond the scope of the present study. As a first step for future improvements, a direction scheme should be defined that allows the estimation of the *MA* with less than the 45 orientation combinations of the tensor direction scheme because only twelve parameters, the three diagonal elements of $\underline{\underline{\mathbf{R}}}$ in the second order and nine elements of $\underline{\underline{\underline{\underline{\tilde{\mathbf{R}}}}}}$ in the fourth order, are required. Although a simple approach would be to involve three acquisitions with a second q value to identify the required second order elements, this can be considered to be less appropriate because unwanted signal variations with q may be present that for instance are observed in standard, single-wave-vector diffusion-weighting experiments of biological tissue [23–25].

The theoretical results provided can also be applied to mixtures of pore ensembles with different sizes or geometries. A weighted mean of the *MA* values can be expected to be observed is such cases. Thus, although the DWV experiment is able to detect a microscopic anisotropy in macroscopic isotropic samples, the signal averaging over the measurement volume or voxel still introduces a bias that may be insolvable with the theoretical framework presented.

Some minor angular modulation was observed for the simulations of spherical pores. It can be conjectured that these deviations are due to rounding errors that may not exactly yield (i) wave vectors with identical magnitudes for the different orientations and (ii) a perfectly spherical or ellipsoidal pore shape. It also may be possible that the hidden algorithm of the random number generator also has some influence on these artifacts. However, these modulations were well below those observed for the ellipsoidal pores and are not expected to have a significant influence on the results. Furthermore, a slight, but systematic underestimation of the pore-size parameters was observed which also has been found in previous studies [12,13]. But because the deviation is typically about 5% or below, this is not considered to be a major problem.

Most likely these deviations are due to higher, i.e. sixth, order contributions. A detailed analysis of the corresponding expressions (sixth order terms of $\tilde{\rho}(\mathbf{q})$, inner- and inter-wave-vector products of third order terms and second with fourth order terms of $\tilde{\rho}(\mathbf{q})$) seems to be tedious but it is evident that only inter-wave-vector products can introduce an (additional) angular modulation. These contributions may distort the angular dependency and the difference between parallel and orthogonal wave vector orientations. But as can be seen in the simulations performed, such effects are not very pronounced (see Fig. 8). Even for a substantial signal decay of, in average, more than 75% the fourth order curve fits the simulated data quite well and reproduces the expected *MA*. Only the slight deviations observed between the simulations and the fit, e.g. for parallel and antiparallel wave vector orientations, may be related to higher order contributions.

More relevant for real experiments seems to be the effect of finite timing parameters, in particular of the gradient pulse duration that may be in the range of tenth of milliseconds on a whole-body MR system. Previous simulations showed a decrease of the signal difference between parallel and orthogonal wave vector orientations for longer pulse durations, e.g. by about 16% for 20 ms-pulses [11]. Taking into account that the *MA* is proportional to the square root of the modulation amplitude, the systematic

underestimation can be expected to be moderate even for whole-body applications. However, if more detailed estimations of these deviations are required, the multiple propagator method [26] may provide a promising framework that also is able to consider finite diffusion and mixing times. Initial results have confirmed the underestimation of the anisotropy at finite pulse durations for ellipsoidal pores [26].

In this context, it could be interesting to extend the presented theory to the use of multiple concatenations of the two wave vectors [13], i.e. to an experiment where more than two diffusion-weighting periods with the first or the second wave vector are applied. Because the diffusion weighting per wave vector can be reduced in such an experiment, shorter gradient pulses can be achieved which may help to improve the detectability of the signal modulation and the accuracy of the derived anisotropy measure, in particular on whole-body MR systems with their limited gradient amplitudes.

It should be noted that the tensor model presented can also be applied to experiments with different wave vector amplitudes ($q_1 \neq q_2$), for instance 2D variants of the DWV experiment. In such experiments the amplitude of both wave vectors is varied [3,27] and typical off-diagonal patterns appear in the Laplace-transformed spectrum if locally anisotropic diffusion is present [27,28]. However, if a macroscopic anisotropy is present, the results of these experiments will depend on the sample's orientation. This problem has been solved for the experiment with constant wave vector amplitudes on the basis of the presented tensor model by using the anisotropy scheme for the wave vector orientations. This approach may also be applicable to the 2D variants of the experiment, i.e. the 15 orientation combinations of the anisotropy scheme could be expected to be, if not the solution, at least a good starting point to obtain orientation-independent results in macroscopically anisotropic samples.

Although the DWV experiment with long mixing times is a promising approach, other methods to assess the diffusion anisotropy on a microscopic level should be kept in mind. First, it can be expected that higher order terms in the DWV experiment with *short* mixing times may also be sensitive to the microscopic diffusion anisotropy. Corresponding experiments can be realized with shorter echo times which would yield an improved signal-to-noise ration, however, it remains to be clarified whether the anisotropy-related modulation amplitude is comparable to the experiment with long mixing times. Furthermore, such an anisotropy-related modulation needs to be detected in a strongly modulated background due to the pore-size dependent second order term that is proportional to $\cos\theta$.

6. Conclusions

A tensor approach to double-wave-vector diffusion-weighting experiments with long mixing times has been presented that describes the signal in the general case of arbitrary cell or pore shapes and orientation distributions. From these equations, a rotationally invariant measure of the microscopic anisotropy can be derived that represents the pore anisotropy independent of the pore orientation distribution and can be determined from a few measurements with different orientations of the two wave vectors. Thus, the presented results may help to improve the reliability and quantifiability of double-wave-vector diffusion-weighting experiments that aim to determine pore or cell eccentricities.

Acknowledgments

This work was supported by the Volkswagenstiftung and the Bundesministerium für Bildung und Forschung (Neuroimage Nord).

Appendix

Applying Eq. (38) and (39) to an isotropic orientation distribution means that each element of the effective tensors needs to be averaged over all possible orientations Ψ' of the cell, e.g.

$$\underline{\underline{\mathbf{R}_{\mathbf{iso}}}} = \int_{\Psi} \underline{\underline{\mathbf{R}}}_{\Psi'} \, d\Psi' \Big/ \int_{\Psi} d\Psi' \tag{A.1}$$

where $\underline{\underline{\mathbf{R}}}_{\Psi'}$ is the tensor $\underline{\underline{\mathbf{R}}}$ for the orientation Ψ'. It should be noted that Ψ' uniquely defines the orientations of all eigenvectors of $\underline{\underline{\mathbf{R}}}$ and not only that corresponding to the largest eigenvalue. It therefore is defined by the three Euler angles that describe the relative orientations of two coordinate systems. $\underline{\underline{\mathbf{R}_{\mathbf{iso}}}}$ can be easily obtained [12] and is given by

$$\underline{\underline{\mathbf{R}_{\mathbf{iso}}}} = \frac{1}{3}\begin{pmatrix} \langle R^2\rangle & 0 & 0 \\ 0 & \langle R^2\rangle & 0 \\ 0 & 0 & \langle R^2\rangle \end{pmatrix} \tag{A.2}$$

with $\langle R^2\rangle = \sum_k R_{kk} = \sum_k R_k = \int_{\text{pore}} r^2 d\mathbf{r}$. Thus, the second order term in Eq. (20) reduces to $-\frac{2}{3}\langle R^2\rangle q^2$ for an isotropic orientation distribution. Furthermore, it is obvious that the anisotropy A defined in Eq. (30) vanishes for $\underline{\underline{\mathbf{R}_{\mathbf{iso}}}}$.

The calculation of $\underline{\underline{\widetilde{\mathbf{R}}_{\mathbf{iso}}}}$ is, although straightforward, more tedious and will not be reproduced in detail here. Without loss of generality, it can be assumed that the orientations Ψ' are considered relative to the eigenvector coordinate system of $\underline{\underline{\mathbf{R}}}$ which means that all elements of $\underline{\underline{\mathbf{R}}}_{\Psi'}$ can be described by the three R_{ii} and the three Euler angles. $\underline{\underline{\widetilde{\mathbf{R}}_{\mathbf{iso}}}}$ then is given by

$$\underline{\underline{\widetilde{\mathbf{R}}_{\mathbf{iso}}}} = \frac{1}{15}\begin{pmatrix} \langle R_{kk}^2\rangle & \langle R_{kk}R_{ll}\rangle & \langle R_{kk}R_{ll}\rangle & 0 & 0 & 0 \\ \langle R_{kk}R_{ll}\rangle & \langle R_{kk}^2\rangle & \langle R_{kk}R_{ll}\rangle & 0 & 0 & 0 \\ \langle R_{kk}R_{ll}\rangle & \langle R_{kk}R_{ll}\rangle & \langle R_{kk}^2\rangle & 0 & 0 & 0 \\ 0 & 0 & 0 & 4\langle R_{kl}^2\rangle & 0 & 0 \\ 0 & 0 & 0 & 0 & 4\langle R_{kl}^2\rangle & 0 \\ 0 & 0 & 0 & 0 & 0 & 4\langle R_{kl}^2\rangle \end{pmatrix} \tag{A.3}$$

with

$$\begin{aligned} \langle R_{kk}^2\rangle &= \int_{\Psi} R_{\Psi',11}^2 \, d\Psi' = 2\sum_k R_{kk}^2 + \sum_{k,l} R_{kk}R_{ll} = 3\sum_k R_{kk}^2 + 2\sum_{\substack{k,l \\ k<l}} R_{kk}R_{ll} \\ \langle R_{kk}R_{ll}\rangle &= \int_{\Psi} R_{\Psi',11}R_{\Psi',22} \, d\Psi' = -\sum_k R_{kk}^2 + 2\sum_{k,l} R_{kk}R_{ll} \\ &= \sum_k R_{kk}^2 + 4\sum_{\substack{k,l \\ k<l}} R_{kk}R_{ll} \\ \langle R_{kl}^2\rangle &= \int_{\Psi} R_{\Psi',12}^2 \, d\Psi' = \frac{3}{2}\sum_k R_{kk}^2 - \frac{1}{2}\sum_{k,l} R_{kk}R_{ll} = \sum_k R_{kk}^2 - \sum_{\substack{k,l \\ k<l}} R_{kk}R_{ll} \end{aligned} \tag{A.4}$$

i.e. (i) all elements $\widetilde{R}_{\text{iso},kl}$ with $k \neq l$ and $\max(k,l) > 3$ vanish and (ii) there are only three different elements. Both findings can also be derived considering the fact that $\underline{\underline{\widetilde{\mathbf{R}}_{\mathbf{iso}}}}$ must be invariant under any rotation.

In Eq. (A.4) it can be seen that the three different elements of $\underline{\underline{\widetilde{\mathbf{R}}_{\mathbf{iso}}}}$ are not independent, e.g.

$$\langle R_{kk}^2\rangle = \langle R_{kk}R_{ll}\rangle + 2\langle R_{kl}^2\rangle, \tag{A.5}$$

and $\underline{\underline{\widetilde{\mathbf{R}}_{iso}}}$ can be re-written to

$$\underline{\underline{\widetilde{\mathbf{R}}_{\mathbf{iso}}}} = \frac{1}{15}\langle R_{kk}R_{ll}\rangle\underline{\underline{\widetilde{\mathbf{P}}_{\mathbf{1}}}} + \frac{2}{15}\langle R_{kl}^2\rangle\underline{\underline{\widetilde{\mathbf{P}}_{\mathbf{2}}}} \tag{A.6}$$

when defining a 3×3 matrix $\underline{\underline{\mathbf{E}}}$ with $E_{ij}=1$ and the 6×6 matrices

$$\underline{\underline{\widetilde{\mathbf{P}}_{\mathbf{1}}}} = \begin{pmatrix} \underline{\underline{\mathbf{E}}} & \underline{\underline{\mathbf{0}}} \\ \underline{\underline{\mathbf{0}}} & \underline{\underline{\mathbf{0}}} \end{pmatrix}$$
$$\underline{\underline{\widetilde{\mathbf{P}}_{\mathbf{2}}}} = \begin{pmatrix} \underline{\underline{\mathbf{1}}} & \underline{\underline{\mathbf{0}}} \\ \underline{\underline{\mathbf{0}}} & 2\underline{\underline{\mathbf{1}}} \end{pmatrix} \tag{A.7}$$

Because

$$\tilde{\mathbf{q}}_v^T\underline{\underline{\widetilde{\mathbf{P}}_{\mathbf{1}}}}\tilde{\mathbf{q}}_\mu^T = (\mathbf{q}_v\cdot\mathbf{q}_v)\left(\mathbf{q}_\mu\cdot\mathbf{q}_\mu\right) = q^4 \tag{A.8}$$

and

$$\tilde{\mathbf{q}}_v^T\underline{\underline{\widetilde{\mathbf{P}}_{\mathbf{2}}}}\tilde{\mathbf{q}}_\mu^T = \left(\mathbf{q}_v\cdot\mathbf{q}_\mu\right)^2 = q^4\cos^2\theta \tag{A.9}$$

for $q_1=q_2=q$ and $\cos\theta=\mathbf{q}_v\cdot\mathbf{q}_\mu/q^2$, i.e. θ being the angle between the two wave vectors, the signal contribution related to $\underline{\underline{\widetilde{\mathbf{R}}_{\mathbf{iso}}}}$ in Eq. (20) yields

$$\begin{aligned}\widetilde{\mathbf{Q}}^T\begin{pmatrix} 3\underline{\underline{\widetilde{\mathbf{R}}_{\mathbf{iso}}}} & 6\underline{\underline{\widetilde{\mathbf{R}}_{\mathbf{iso}}}} \\ 6\underline{\underline{\widetilde{\mathbf{R}}_{\mathbf{iso}}}} & 3\underline{\underline{\widetilde{\mathbf{R}}_{\mathbf{iso}}}}\end{pmatrix}\widetilde{\mathbf{Q}} &= \frac{1}{5}\left(\langle R_{kk}R_{ll}\rangle q^4 + 2\langle R_{kl}^2\rangle q^4\right)\\ &+\frac{2}{5}\left(\langle R_{kk}R_{ll}\rangle q^4 + 2\langle R_{kl}^2\rangle q^4\cos^2\theta\right)\\ &+\frac{2}{5}\left(\langle R_{kk}R_{ll}\rangle q^4 + 2\langle R_{kl}^2\rangle q^4\cos^2\theta\right)\\ &+\frac{1}{5}\left(\langle R_{kk}R_{ll}\rangle q^4 + 2\langle R_{kl}^2\rangle q^4\right) = \frac{6}{5}\langle R_{kk}R_{ll}\rangle q^4\\ &+\frac{4}{5}\langle R_{kl}^2\rangle q^4(2+\cos 2\theta)\end{aligned}$$

Thus, a dependency of the signal on the angle θ between the two wave vectors with $\cos 2\theta$ is obtained.

Analogously, $\underline{\underline{\widetilde{\mathbf{S}}_{\mathbf{iso}}}}$ can be calculated yielding

$$\underline{\underline{\widetilde{\mathbf{S}}_{\mathbf{iso}}}} = \frac{1}{15}\begin{pmatrix} \langle S_{kkkk}\rangle & \langle S_{kkll}\rangle & \langle S_{kkll}\rangle & 0 & 0 & 0\\ \langle S_{kkll}\rangle & \langle S_{kkkk}\rangle & \langle S_{kkll}\rangle & 0 & 0 & 0\\ \langle S_{kkll}\rangle & \langle S_{kkll}\rangle & \langle S_{kkkk}\rangle & 0 & 0 & 0\\ 0 & 0 & 0 & 4\langle S_{kkll}\rangle & 0 & 0\\ 0 & 0 & 0 & 0 & 4\langle S_{kkll}\rangle & 0\\ 0 & 0 & 0 & 0 & 0 & 4\langle S_{kkll}\rangle\end{pmatrix} \tag{A.11}$$

with $\langle S_{kkkk}\rangle = 3\langle R^4\rangle$, $\langle R^4\rangle = \int r^4\,d\mathbf{r}$, and $\langle S_{kkll}\rangle = \langle R^4\rangle$. Thus,

$$\underline{\underline{\widetilde{\mathbf{S}}_{\mathbf{iso}}}} = \frac{1}{5}\langle R^4\rangle\left(\underline{\underline{\widetilde{\mathbf{P}}_{\mathbf{1}}}} + 2\underline{\underline{\widetilde{\mathbf{P}}_{\mathbf{2}}}}\right) \tag{A.12}$$

and the fourth order signal contribution related to $\underline{\underline{\widetilde{\mathbf{S}}_{\mathbf{iso}}}}$ can be written as

$$\widetilde{\mathbf{Q}}^T\begin{pmatrix} \underline{\underline{\widetilde{\mathbf{S}}_{\mathbf{iso}}}} & \underline{\underline{\mathbf{0}}} \\ \underline{\underline{\mathbf{0}}} & \underline{\underline{\widetilde{\mathbf{S}}_{\mathbf{iso}}}}\end{pmatrix}\widetilde{\mathbf{Q}} = \frac{6}{5}\langle R^4\rangle q^4 \tag{A.13}$$

In summary, the signal for an isotropic orientation distribution of the cells and $q_1=q_2=q$ can be written as

$$\begin{aligned}M_{\mathrm{iso}}(q,\theta) &\propto 1 - \frac{2}{3}\langle R^2\rangle q^2\\ &+\left[\frac{1}{30}\left(3\langle R^4\rangle + 3\langle R_{kk}R_{ll}\rangle + 4\langle R_{kl}^2\rangle\right) + \frac{1}{15}\langle R_{kl}^2\rangle\cos 2\theta\right]q^4\\ &= 1 - \frac{2}{3}\langle R^2\rangle q^2 + \frac{1}{30}\left[3\langle R^4\rangle + 2\langle R_{kk}^2\rangle + \langle R_{kk}R_{ll}\rangle\right.\\ &+\left.\left(\langle R_{kk}^2\rangle - \langle R_{kk}R_{ll}\rangle\right)\cos 2\theta\right]q^4\end{aligned}$$

MA for an isotropic orientation distribution, i.e. with $\underline{\underline{\widetilde{\mathbf{R}}_{\mathbf{iso}}}}$ according to Eqs. (29) and (A.3), yields

$$\begin{aligned}MA &= \sqrt{\frac{1}{5}\langle R_{kk}^2\rangle - \frac{1}{5}\langle R_{kk}R_{ll}\rangle + \frac{3}{5}\langle R_{kl}^2\rangle}\Big/\langle R^2\rangle\\ &= \sqrt{\sum\nolimits_k R_{kk,\Psi'=0} - \sum\nolimits_{k,l\,k<l} R_{kk,\Psi'=0}R_{ll,\Psi'=0}}\Big/\sum_k R_{kk,\Psi'=0}\end{aligned} \tag{A.15}$$

which is identical to the value that would be obtained for a single pore orientation ($R_{kl}=0$ for $k\neq l$ and $\Psi'=0$, i.e. in the chosen coordinate system). Furthermore, taking the relationship of Eq. (A.5) into account, it can be seen that it is proportional to the square root of the modulation amplitude of Eq. (44):

$$\begin{aligned}MA &\propto \sqrt{\frac{1}{5}\langle R_{kk}^2\rangle - \frac{1}{5}\langle R_{kk}R_{ll}\rangle + \frac{3}{5}\langle R_{kl}^2\rangle} = \sqrt{\langle R_{kl}^2\rangle}\\ &= \sqrt{\frac{1}{2}\left(\langle R_{kk}^2\rangle - \langle R_{kk}R_{ll}\rangle\right)}.\end{aligned} \tag{A.16}$$

References

[1] P.P. Mitra, Multiple wave-vector extensions of the NMR pulsed-field-gradient spin–echo diffusion measurement, Phys. Rev. B 51 (1995) 15074–15078.
[2] D.G. Cory, A.N. Garroway, J.B. Miller, Applications of spin transport as a probe of local geometry, Polym. Preprints 31 (1990) 149–150.
[3] P.T. Callaghan, B. Manz, Velocity exchange spectroscopy, J. Magn. Reson. A 106 (1994) 260–265.
[4] P.T. Callaghan, D. MacGowan, K.J. Packer, F.O. Zelayam, High-resolution q-space imaging in porous structures, J. Magn. Reson. 90 (1990) 177–182.
[5] E.O. Stejskal, J.E. Tanner, Spin diffusion measurements: spin–echoes in the presence of a time-dependent field gradient, J. Chem. Phys. 42 (1965) 288–292.
[6] M.A. Koch, J. Finsterbusch, Compartment size estimation with double wave vector diffusion-weighted imaging, Magn. Reson. Med. 60 (2008) 90–101.
[7] T. Weber, C.H. Ziener, T. Kampf, V. Herold, W.R. Bauer, P.M. Jakob, Measurement of apparent cell radii using a multiple wave vector diffusion experiment, Magn. Reson. Med. 61 (2009) 1001–1006.
[8] M.A. Koch, J. Finsterbusch, Double wave vector diffusion weighting in the human corticospinal tract in vivo, in: Proceedings, Int. Soc. Magn. Reson. Med., 16th Annual Meeting, Toronto, Canada, 2008, p. 764.
[9] M.A. Koch, J. Finsterbusch, Trace weighting in double wave vector diffusion experiments in vivo, in: Proceedings, Int. Soc. Magn. Reson. Med., 17th Annual Meeting, Honolulu, Hawaii, USA, 2009, p. 1362.
[10] E. Özarslan, P.J. Basser, Microscopic anisotropy revealed by NMR double pulsed field gradient experiments with arbitrary timing parameters, J. Chem. Phys. 128 (2008) 154511-1–154511-11.
[11] M.A. Koch, J. Finsterbusch, Numerical simulation of double wave vector experiments investigating diffusion in randomly oriented ellipsoidal pores, Magn. Reson. Med. 62 (2009) 247–254.
[12] J. Finsterbusch, M.A. Koch, A tensor approach to double wave vector diffusion-weighting experiments on restricted diffusion, Magn. Reson. Med. 195 (2008) 23–32.
[13] J. Finsterbusch, Extension of the double-wave-vector diffusion-weighting experiment to multiple concatenations, J. Magn. Reson. 198 (2009) 174–182.
[14] Y. Cheng, D.G. Cory, Multiple scattering by NMR, J. Am. Chem. Soc. 121 (1999) 7935–7936.
[15] P.T. Callaghan, M.E. Komlosh, Locally anisotropic motion in a macroscopically isotropic system: displacement correlations measured using double pulsed gradient spin–echo NMR, Magn. Reson. Chem. 40 (2002) S15–S19.
[16] Y. Qiao, P. Galvosas, P.T. Callaghan, Diffusion correlation NMR spectroscopic study of anisotropic diffusion of water in plant tissues, Biophys. J. 89 (2005) 2899–2905.
[17] M.E. Komlosh, F. Horkay, R.Z. Freidlin, U. Nevo, Y. Assaf, P.J. Basser, Detection of microscopic anisotropy in gray matter and in a novel tissue phantom using double pulsed gradient spin–echo MR, J. Magn. Reson. 189 (2007) 38–45.
[18] M.E. Komlosh, M.J. Lizak, F. Horkay, R.Z. Freidlin, P.J. Basser, Observation of microscopic diffusion anisotropy in the spinal cord using double-pulsed gradient spin–echo MRI, Magn. Reson. Med. 59 (2008) 803–809.
[19] E. Özarslan, Compartment shape anisotropy (CSA) revealed by double pulsed gradient field MR, J. Magn. Reson. 199 (2009) 56–67.
[20] B.A. Auld, Acoustic Fields and Waves in Solids, vol. I, Wiley Interscience, New York, 1973.
[21] P.B. Kingsley, Introduction to diffusion tensor imaging mathematics: Part III, Concepts Magn. Reson. A 28A (2006) 155–179.
[22] P.J. Basser, C. Pierpaoli, Microstructural and physiological features of tissues elucidated by quantitative-diffusion-tensor MRI, J. Magn. Reson. B 111 (1996) 209–219.
[23] M.A. Horsfield, G.J. Barker, W.I. McDonald, Self-diffusion in CNS tissue by volume-selective proton NMR, Magn. Reson. Med. 31 (1994) 637–644.

[24] T. Niendorf, R.M. Dijkhuizen, D.G. Norris, M. van Lookeren Campagne, K. Nicolay, Biexponential diffusion attenuation in various states of brain tissue: implications for diffusion-weighted imaging, Magn. Reson. Med. 36 (1996) 847–857.
[25] Y. Assaf, Y. Cohen, Non-mono-exponential attenuation of water and *N*-acetyl aspartate signals due to diffusion in brain tissue, J. Magn. Reson. 131 (1998) 69–85.
[26] E. Özarslan, N. Shemesh, P.J. Basser, A general framework to quantify the effect of restricted diffusion on the NMR signal with applications to double pulsed field gradient NMR experiments, J. Chem. Phys. 130 (2009) 104702.
[27] P.T. Callaghan, S. Godefroy, B.N. Ryland, Use of the second dimension in PGSE NMR studies of porous media, Magn. Reson. Imaging 21 (2003) 243–248.
[28] P.T. Callaghan, I. Furó, Diffusion–diffusion correlation and exchange as a signature for local order and dynamics, J. Chem. Phys. 120 (2004) 4032–4038.